nature neuroscience

Technical Report

https://doi.org/10.1038/s41593-025-02127-6

Patterned wireless transcranial optogenetics generates artificial perception

Received: 4 March 2024

Accepted: 10 October 2025

Published online: 8 December 2025

Check for updates

Mingzheng Wu[1,2,23], Yiyuan Yang[1,3,4,5,6,23] ✉, Jinglan Zhang[2,23], Andrew I. Efimov[1,7,23], Xiuyuan Li[8,9,23], Kaiqing Zhang[8,10,23], Yue Wang[1,7], Kevin L. Bodkin[2], Mohammad Riahi[11,12], Jianyu Gu[1], Glingna Wang[1,13], Minsung Kim[1], Liangsong Zeng[1,3], Jiaqi Liu[1], Lauren H. Yoon[2,14], Haohui Zhang[8], Sara N. Freda[2], Minkyu Lee[1], Jiheon Kang[1], Joanna L. Ciatti[1,15], Kaila Ting[1], Stephen Cheng[1], Xincheng Zhang[16], He Sun[16], Wenming Zhang[9], Yi Zhang[16], Anthony Banks[1,17,18], Cameron H. Good[1,17,18], Julia M. Cox[19,20], Lucas Pinto[2,19,20], Abraham Vázquez-Guardado[1,11,12] ✉, Yonggang Huang[1,3,8,15] ✉, Yevgenia Kozorovitskiy[2,21] ✉ & John A. Rogers[1,3,7,15,17,22] ✉

Synthesizing perceivable artificial neural inputs independent of typical sensory channels remains a fundamental challenge in developing next-generation brain–machine interfaces. Establishing a minimally invasive, wirelessly effective and miniaturized platform with long-term stability is crucial for creating research methods and clinically meaningful biointerfaces capable of mediating artificial perceptual feedback. Here we demonstrate a miniaturized, fully implantable transcranial optogenetic neural stimulator designed to generate artificial perceptions by patterning large cortical ensembles wirelessly in real time. Experimentally validated numerical simulations characterized light and heat propagation, whereas neuronal responses were assessed by in vivo electrophysiology and molecular methods. Cue discrimination during operant learning demonstrated the wireless genesis of artificial percepts sensed by mice, where spatial distance across large cortical networks and sequential order-based analyses of discrimination predicted performance. These conceptual and technical advances expand understanding of artificially patterned neural activity and its perception by the brain to guide the evolution of next-generation all-optical brain–machine communication.

Creating artificial connections between the brain and the external world is becoming possible with recent advances in neuroscience and neurotechnology[1–3]. The establishment of independent input channels bypassing the typical sensory pathways enables effective brain–machine communication, allowing healthy or sensory-impaired individuals to augment sensation[4,5]. Reliable biointegrated neurotechnologies incorporating wireless communication in minimally invasive implantable form factors are required to serve as functional interfaces that deliver information to the brain in real time. Most current and envisioned brain–machine interfaces (BMIs) consist of intricate setups that disrupt natural behavior, lack cell-type-specific capabilities and struggle to achieve sustained long-term operation in biological systems[6].

In this study, we developed a fully implantable wireless transcranial optogenetic platform to generate artificial perceptions through spatiotemporally controlled optogenetic stimulation among distributed cortical regions in untethered mice. To our knowledge,

A full list of affiliations appears at the end of the paper. ✉e-mail: yyy@nus.edu.sg; abraham.vg@ncsu.edu; y-huang@northwestern.edu; yevgenia.kozorovitskiy@northwestern.edu; jrogers@northwestern.edu

this combination of features has not yet been achieved, although it leverages previous important advances incorporating subsets of these properties in freely moving animals[7–11]. This platform complements previous studies using advanced multiphoton microscopy and holographic optogenetics to elaborate the processing of artificial inputs within cortical or hippocampal regions at cellular resolution in head-fixed animals[12–19].

In addition, higher-order cognitive behaviors emerge from multimodal brain-wide dynamics[20–23], yet how cortex-wide, artificially patterned activity is perceived remains unknown. Here, the generation of synthetic perceptions relies on large-scale sequential cortical activation, where the spatiotemporal patterns of cortical activity represent cues for mice to make decisions in an operant learning paradigm. The spatial distance among activated cortical area sequences determines the discriminability of synthesized perceptions, captured in behavioral outcomes. This work introduces a unique wireless transcranial stimulator and provides a foundational framework for expanding brain–machine communication into a broader cognitive domain through patterned cortical activation. This technology is compatible with standard manufacturing in flexible electronics industrial processes and does not require sophisticated clean room microfabrication facilities, improving adaptability and scalability for broad dissemination in the neuroscience and BMI communities.

Results

Engineering platform for dynamic wireless transcranial perception modulation

The fully implantable wirelessly radiofrequency-powered transcranial optogenetic stimulator features an array of microscale inorganic light-emitting diodes (μ-ILEDs, 300 × 300 × 90 μm^3) with independent, real-time wireless control over patterned optogenetic modulation of neuronal activity. The platform employs multilayer copper–polymer flexible printed circuit board (fPCB) as a base of the device layout and serves as the substrate for electronic components. This scheme eliminates the need for complex processes in microfabrication, and it provides an immediate path to scale-up manufacture and broad distribution[8,24] (Extended Data Fig. 1). The modular design consists of a flexible optogenetic display (FOD) based on a programmable array of μ-ILEDs and a wireless control module connected through a set of mechanically compliant thin serpentine traces (Fig. 1a). A conformal coating of parylene-C (14 μm) symmetrically encapsulates and isolates the electronic components, FOD and serpentine traces from the in vivo biofluidic environment. An additional coating of a soft silicone elastomer (400 μm, Young's modulus: approximately 60 kPa) creates a compliant device–tissue interface. This coating also provides further mechanical support to the serpentine connections to improve their resilience to stretching and bending, thereby ensuring stable operation during repetitive cycles of deformations induced by natural motions of the animal.

This FOD can target selected, spatially separated groups of neurons in the cerebral cortex through transcranial optogenetic stimulation. The wireless control module is designed to reside at the lumbar spine level in a mouse, utilizing the broad subdermal space to house the receiver antenna and electronic components for continuous wireless power supply and dynamic independent control over individual μ-ILEDs in the FOD (Fig. 1b). The FOD is scalable in the density and geometric patterns of μ-ILEDs to target user-defined cortical regions (here, up to 64 in an 8 × 8 configuration; Fig. 1c,d and Supplementary Video 1). With the 8 × 8 density of μ-ILEDs, up to $2^{64} - 1$ spatial patterns can be generated, with a parameter set that becomes uncountably large with variations in temporal patterning. The wireless optogenetic stimulator uses magnetic inductive power transfer between resonant transmission and receiver antennas operating at the industrial, scientific and medical radiofrequency (ISMRF) band (13.56 MHz), located around the experimental enclosure and device perimeter, respectively. The combination of a near-field communication (NFC) system-on-a-chip and a microcontroller, equipped with a dedicated firmware, facilitates remote on/off (Supplementary Video 2) and intensity control over individual μ-ILEDs (Supplementary Video 3). This is achieved with a hybridized analog/digital matrix multiplexing approach (Fig. 1e) through a library application programming interface in MATLAB (MathWorks). The encoded spatiotemporal patterns of illumination deliver digitized stimulation inputs to the brain. In addition, the programmable intensity of μ-ILEDs adds another degree of freedom to control the illumination volume of targeted cortical areas. Similar to a previously reported design with a single μ-ILED[9], a collection of ceramic capacitors (5 × 22 μF, approximately 1.37 mJ at 5 V) with low internal resistances enables fast discharge dynamics to provide short transcranial optical pulses (for example, 2 ms) at high intensity (up to approximately 70 mW mm^{-2}) with rapid charge replenishment. Integrating this technology with open-source behavioral systems provides reconfigurable stimulation patterns driven by real-time behavioral outcomes. Experimenters can further evaluate perceptual responses to digitized cortical activation through diverse cue-based operant learning paradigms, where mice detect or distinguish among artificial percepts to seek external rewards (Fig. 1e).

The thin, subdermal implantable design enables application in small animal models (for example, mice; Fig. 1f) as a fully implanted device, without affecting their natural behavior in complex experimental environments (Fig. 1g). Furthermore, iterative simulation-guided optimization of the geometries and the multilayer configurations of the serpentine interconnects ensure robust operation, without fracture or fatigue in the constituent materials (Supplementary Methods and Extended Data Fig. 2a–i). The optimization increases the effective serpentine stretchability from 7% (basic design) to 28% (optimized design) (Extended Data Fig. 2j–l). Benchtop cyclic stretching and bending tests validate these enhancements, with the conductance stability improving from 1,000 cycles (basic design) to at least 20,000 cycles (optimized design) (Extended Data Fig. 2m–o). The longevity of the resulting devices meets practical requirements of long-term experimental protocols (Extended Data Fig. 2p). The overall design allows straightforward adaptations to accommodate other experimental models, ranging from rodents to non-human primates. Further details on device fabrication, electronic modules and implantation procedures appear in Extended Data Fig. 3, Methods and Supplementary Methods. Supplementary Table 1 provides a detailed comparison of this technology to relevant previous engineering approaches, highlighting the unique capabilities of the current device for dynamic cortex-wide neuromodulation in untethered, freely moving animals.

Spatiotemporal characteristics of light propagation and heat generation

A comprehensive understanding of transcranial light propagation through the brain is essential for assessing the biological impact of optical neuromodulation[25]. Moreover, the potential off-target opsin-independent effects, such as heat accumulation, are key considerations in preventing unintended changes in neuronal activity[26]. Light absorption by the brain tissue and Joule heating of the μ-ILEDs contribute to thermal stress in the illuminated and adjacent regions (Fig. 2a). Operation of multiple μ-ILEDs leads to additive effects in the spatiotemporal domain, requiring additional consideration in the geometric design of the devices and stimulation parameters in experiments. The effects of light and heat propagation can be captured by three-dimensional numerical simulations that use a comprehensive anatomy-guided model that includes the skull, cerebrospinal fluid, brain tissue, device materials and surgical implantation materials (for example, cyanoacrylate adhesive and dental cement) (Fig. 2b). A combination of constitutive properties of the materials and performance characteristics of the μ-ILEDs serves as inputs to this model (Fig. 2c, Extended Data Fig. 4a–e and Supplementary Tables 2 and 3).

A Monte Carlo simulation of the light penetration profile was used to predict the irradiance distribution relative to the coronal section

https://doi.org/10.1038/s41593-025-02127-6

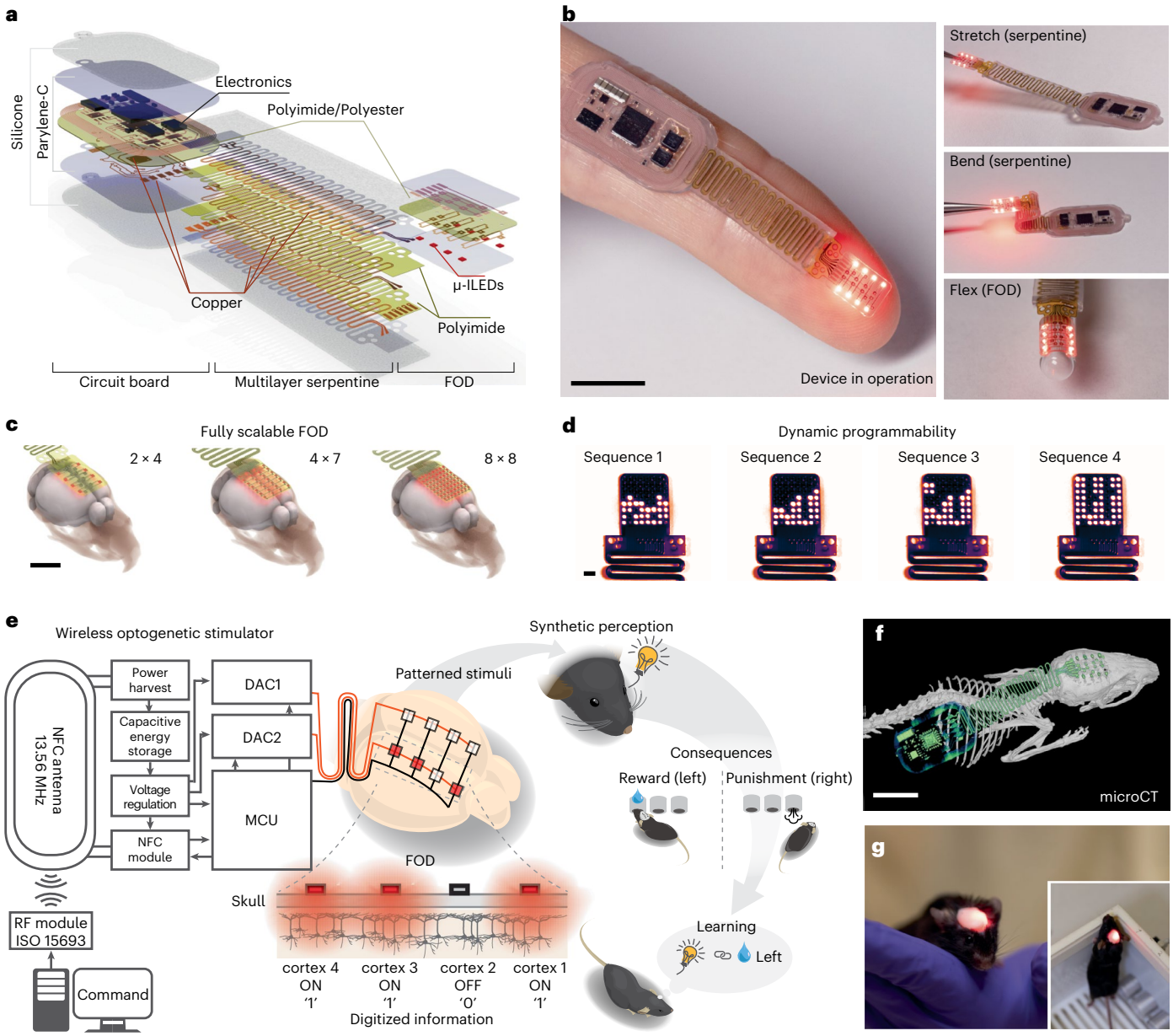

Fig. 1 | Engineering platform for dynamic wireless transcranial perception modulation. a, Layered schematic illustration of a wireless optogenetic encoder for dynamic transcranial control of large-scale cortical activation. **b**, Left: image of the FOD in operation. Right: images showing the controlled patterns of μ-ILEDs during applied deformation of serpentine interconnects and FOD. Scale bar, 10 mm. **c**, Three-dimensional models showing scalable FODs with increasing μ-ILED density to interface with user-defined cortical regions. Scale bar, 5 mm. **d**, Example patterns generated on an 8 × 8 FOD showing dynamic programmability for complex stimulation. Scale bar, 1 mm. **e**, Schematic illustrations of the electronic modules and FOD that enable dynamic perception modulation in the context of learning. **f**, MicroCT image of the wireless optogenetic stimulator implanted in a C57/BL6J mouse. Scale bar, 10 mm. **g**, Close-up photograph showing a device-integrated mouse close to an electromagnetic field resonating at 13.56 MHz. Inset: a device-integrated mouse behaving in the experimental arena circulated by a transmission antenna. RF, radiofrequency; MCU, microcontroller unit.

of the mouse brain based on the Common Coordinate Framework[27] (Fig. 2d). Light intensity measurements with an optical fiber at varying distances to the skull-mounted μ-ILED confirm the simulated attenuation profiles in the brain (normalized intensity at pia as 100%; Fig. 2e and Extended Data Fig. 4f,g). The results model the depth and volume for optogenetic activation of ChrimsonR (628 nm; irradiance threshold of 1 mW mm^{-2})[28] resulting from 6.12-mW optical power provided by a single μ-ILED (Extended Data Fig. 4h). Related simulations were used to predict three-dimensional light propagation profiles for the simultaneous operation of various combinations of multiple μ-ILEDs. As an example, Fig. 2f,g and Extended Data Fig. 4i show co-activation volumes and overlapping fractions from four μ-ILEDs for different optical power inputs and irradiance thresholds (0.1–1 mW mm^{-2}). These numerical modeling approaches can support device design with μ-ILEDs at different wavelengths, providing the basis for calibrating the system for diverse opsins.

Finite element analysis (FEA) techniques reveal transient heat generation and transport dynamics that provide guidelines for selecting operating parameters (power and duty cycle of the μ-ILEDs) to ensure that the maximum temperature rise in the brain remains within a physiologically acceptable range. For optogenetic activation of red-shifted excitatory opsin variants (for example, ChrimsonR), a 2-ms pulse width is sufficient to generate action potentials in stimulated neurons, based on previous studies[9,28]. Operating μ-ILEDs with a 2-ms pulse width at a

https://doi.org/10.1038/s41593-025-02127-6

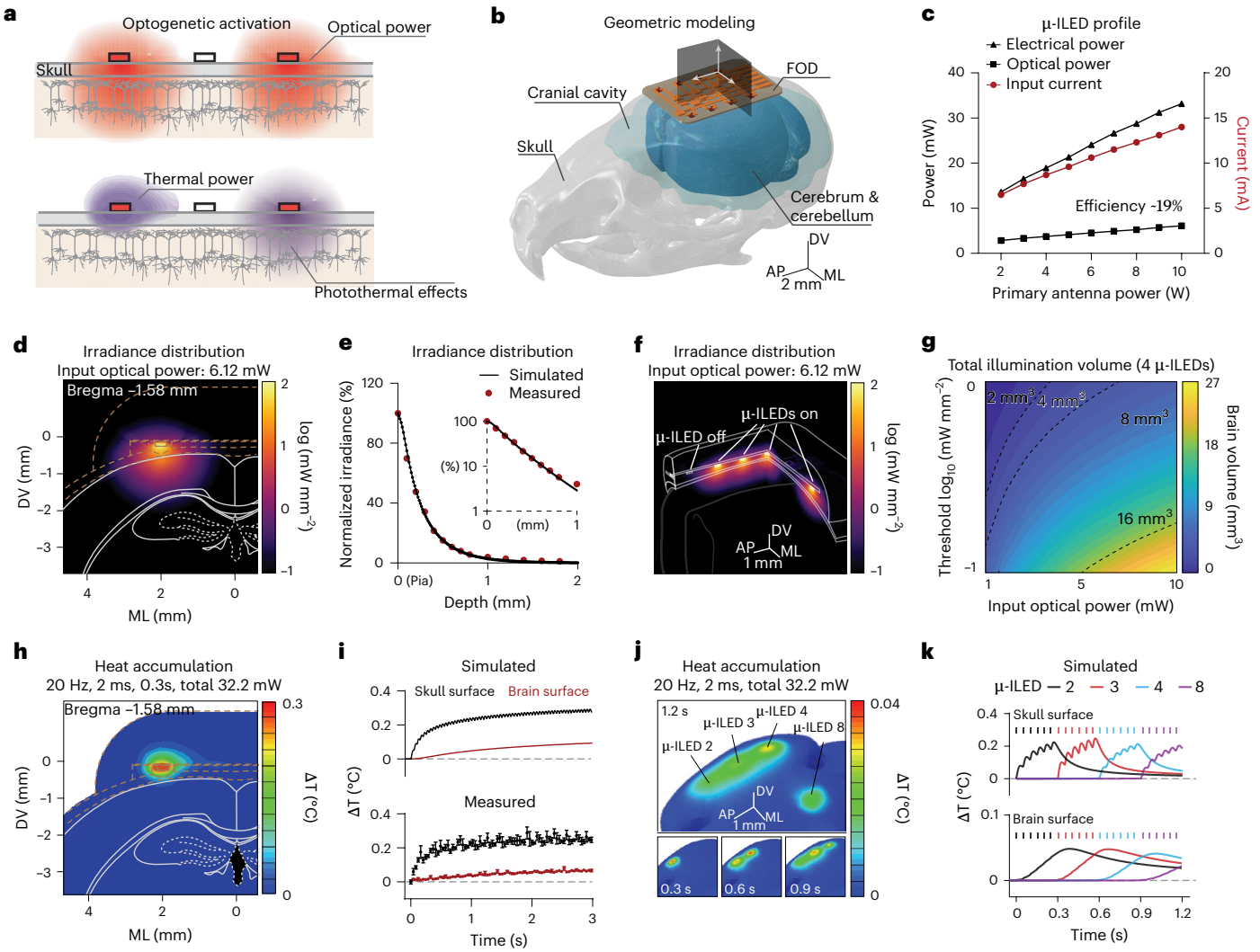

Fig. 2 | Spatiotemporal characteristics of light propagation and heat accumulation during device operation. a, Power conversion pathways in the FOD, including the desired optical power for optogenetic activation, the non-optical power dissipating non-radiatively as heat and the photothermal effects induced by tissue absorption of photons. Cartoon illustration, not reflecting precise scaling factors. **b**, Geometric model of the main components surrounding the FOD. Accessory components, including dental cement, device encapsulations and cyanoacrylate adhesive, are considered in the model but not displayed. Shading areas define the planes of interest in the simulations. **c**, Electrical power, optical power and input current for a single red μ-ILED (628 nm) as a function of primary power applied to the transmission antenna. **d**, Coronal section of three-dimensional Monte Carlo simulation of light propagation from a single μ-ILED relative to the brain regions defined by reference brain atlas at bregma −1.58 mm. Input optical power of μ-ILED, 6.12 mW. **e**, Summary data showing normalized simulated and measured optical intensity at different depths in the brain tissue. Absolute light intensity at 628 nm at different depths was normalized to the maximal intensity at pia ($z = 0$). **f**, Monte Carlo simulation of light propagation of four independent μ-ILEDs in three-dimensional space. Gray lines depict adjacent structures, including dental cement, FOD, encapsulation, cyanoacrylate adhesive and skull and brain surfaces. **g**, Contour map plot showing the total illumination volume from four-μ-ILED co-activation for different input irradiance and intensity thresholds for opsin variants. **h**, Spatial distribution of heat accumulation during a single μ-ILED operation at 20 Hz (2-ms pulse width) for 0.3 seconds in the coronal section. **i**, Simulated and measured temperature rise as a function of operation time at 20 Hz (2-ms pulse width) on the skull and brain surfaces. Measured data are presented as mean ± s.e.m. $n = 5$ technical replicates for skull surfaces; $n = 3$ technical replicates for brain surface. Technical replicates are included to account for fluctuations in environmental temperature. **j**, Spatial distribution of heat generation on the brain surface with sequential four-μ-ILED operation at 20 Hz (2-ms pulse width, 0.3 seconds each). **k**, Simulated temperature rise as a function of operation time at 20 Hz (2-ms pulse width) on the skull and brain surfaces for four individual μ-ILEDs. ~, approximately.

frequency of 20 Hz corresponds to a 4% duty cycle. A three-dimensional FEA thermal simulation based on these illumination parameters models temperature distributions throughout surrounding structures for the operation of a single μ-ILED for 0.3 seconds (20 Hz, 2 ms, six pulses; parameters used in the behavioral experiments below). The results indicate a maximal temperature increase on the skull and brain surfaces at 0.24 °C and 0.04 °C, respectively (Fig. 2h). Temperature monitoring using customized thin-film thermistors is consistent with the simulated temperature increases (Fig. 2i and Extended Data Fig. 5a–c). The dental cement that surrounds the interface promotes the dissipation of heat due to its higher thermal conductivity (approximately 0.7 mW mm^{-1} K^{-1}; Supplementary Table 3) compared to that of adjacent tissue (<0.6 mW mm^{-1} K^{-1}; Supplementary Table 3). The results also capture the temporal dynamics of temperature distributions (Fig. 2i). An example in three-dimensional space involves the activation of multiple μ-ILEDs in sequence (four μ-ILEDs, 0.3 seconds each for a total of 1.2 seconds; parameters used in behavior experiments below) to illustrate the spatiotemporal profile of heat generation across the regions of interest (ROIs) (Fig. 2j). At optical powers similar to those used for behavioral studies below, thermal interference across

multiple µ-ILEDs is minimal (Fig. 2k and Supplementary Video 4). Extended Data Fig. 5d–g shows the simulated and measured temperature rise on the skull and brain surfaces for a single µ-ILED operating with different duty cycles, frequency and input optical power. Simple modifications to the device design, such as the addition of a metal coating on the backside of the FOD, can enhance thermal dissipation (Extended Data Fig. 5h,i), to further reduce the thermal load on the brain, as might be necessary for experimental protocols using high duty cycle optogenetic stimulation. Additional details on numerical characterization and simulation of optical and thermal effects are included in the Methods section. The optical and thermal properties of materials are included in Supplementary Tables 2 and 3.

Characterizing neuronal effects of transcranial optogenetic activation

Our numerical framework predicts effective light transmission through the skull and brain tissue from the µ-ILED light source to activate red-shifted opsin variants. However, the neuronal effects of one-photon optogenetic stimulation do not strictly adhere to the light propagation rules defined by Monte Carlo simulations. The discrepancy may arise from several factors, including the anatomical distribution of neurons across cortical layers, the morphology of targeted neuron subtypes as well as the local irradiance and opsin molecule distribution across subcellular compartments, such as dendritic arbors, neuronal somata and axons. To characterize the neuronal effects of transcranial optogenetic activation, we used illumination from the µ-ILED source in conjunction with AAV.hSyn.ChrimsonR.tdT, which expresses ChrimsonR–tdTomato under the human synapsin 1 (hSyn) gene promoter for high neuron-specific expression. This viral construct does not include specific subcellular targeting motifs, resulting in relatively broad membrane expression patterns.

We transduced AAV.hSyn.ChrimsonR.tdT into eight cortical sites spanning four distinct regions in both hemispheres in adult mice. These regions include the motor cortex (AP: +1.5 mm, ML: ±2.0 mm), somatosensory cortex encompassing the limb regions (AP: 0 mm, ML: ±2.0 mm), somatosensory cortex encompassing the trunk representation (AP: −1.5 mm, ML: ±2.0 mm) and the visual cortex (AP: −3.0 mm, ML: ±2.0 mm) (Fig. 3a and Extended Data Fig. 6a–d). Figure 3b illustrates the targeted brain regions relative to the µ-ILED location in a 2 × 4 FOD configuration. Fluorescence in situ hybridization (FISH) for *tdT*, *Slc32a1*(VGluT1) and *Slc17a7*(VGAT) was used to determine the number of ChrimsonR-expressing neurons and the proportion of excitatory and inhibitory populations (Extended Data Fig. 6c). Our results show that the majority of neurons labeled by our procedures reside in cortical layers 5–6 and are predominantly glutamatergic (*vglut1*$^+$; Fig. 3c).

Next, we examined the mRNA levels for the immediate-early gene *fos* to quantify the extent of neuronal activation in response to optogenetic stimulation from the pulsed µ-ILED light source. *Fos* is known for its rapid-onset transcriptional activity and transient presence, due to its short half-life. Anesthetized ChrimsonR-expressing animals received four 5-minute sessions of optogenetic stimulation (5 seconds on/off, 20 Hz, 2-ms pulse width at 6.12 mW optical power during the 5-second on period) and remained anesthetized before tissue processing to minimize non-stimulation-related *fos* transcription. For each cortical region, two control brain areas were selected: the contralateral region in the opposite hemisphere and a distal contralateral region 3 mm away. A 240 × 240 × 240 µm^3 volume directly beneath the µ-ILED was examined in layer 5 for each cortical region, and every other brain section was sampled for analysis (Fig. 3d). The number of *fos*$^+$ cells in the stimulated region ranged from 42 to 76 (20–46 *tdTomato*$^+$ and 22–44 *tdTomato*$^-$), showing a substantial increase compared to either control region (Fig. 3e).

Although *fos* measures provide a useful quantitative estimate of the number of neurons that have been recently activated and their layer distribution, in vivo extracellular electrophysiology is necessary to sample the temporal patterns of optogenetically evoked neuronal firing under the µ-ILED and at varying distances away, across relevant stimulation intensities (Fig. 3f). Using four-shank, 64-channel multielectrode array (MEA), we recorded extracellular electrical activity in the somatosensory cortex in head-fixed mice (Fig. 3g). We activated a µ-ILED next to the MEA at varying distances along the surface of the cranium. At each distance, 2-ms pulses at 4 Hz were delivered for 60 seconds at 2.20-mW, 4.46-mW, 6.49-mW and 8.07-mW optical power, corresponding to 5-mA, 10-mA, 15-mA and 20-mA input current. We observed evoked single-unit activity time-locked with optogenetic stimulation (Fig. 3h). Figure 3i captures the average firing rate of units at different input irradiance across cortical depth, and Fig. 3j shows the distribution of the firing rate of all recorded single units at different depths before and after optogenetic stimulation at 6.49 mW. For any device that includes multiple spatially distributed light sources, it is essential to characterize the lateral spatial profile of neuronal activation resulting from a single source stimulation. Figure 3k shows the post-stimulation firing rate of cortical units recorded from electrodes placed at different horizontal distances from the µ-ILED with 6.49-mW

Fig. 3 | Characterization of neuronal effects of transcranial optogenetic stimulation via µ-ILEDs. a, Schematic showing viral transduction and stereotaxic coordinates for eight cortical regions in wild-type mice. **b**, Schematic representation of reference brain atlas sections transduced with ChrimsonR, aligned with the µ-ILEDs on a 2 × 4 FOD. **c**, Left: representative image showing the distribution of *tdTomato* (*tdT*), *slc32a1* (*vglut1*) and *slc17a7* (*vgat*) transcripts in superficial and deep layers of the motor cortex. Right: quantification of *tdT*$^+$, *tdT*$^+$*vglut*$^+$ and *tdT*$^+$*vgat*$^+$ cells across cortical regions. $n = 3$ animals per group, mean ± s.e.m. Scale bar, 20 µm. **d**, Top: schematic illustration of the transcranial optogenetic stimulation setup, parameters and sampled brain regions for *fos* transcript quantification. Bottom: representative images of *tdT* and *fos* transcripts in the stimulated cortical region and a distal control region. Scale bar, 20 µm. The experiment was repeated independently on 12 brain slices from three animals. **e**, Left: scatter plots showing integrated density of *tdT* and *fos* transcripts of cells in the stimulated, contralateral control and distal control cortical regions. Thresholds determined by *k*-means clustering, *tdT*$^+$ = 2290.8; *fos*$^+$ = 880.61. Right top: summary of the number of *tdT*$^+$*fos*$^+$ neurons in the stimulated, contralateral control and distal control cortical regions (Stim., 30.25 ± 5.573; Contra, 7.25 ± 3.544; Distal, 2.5 ± 0.866; one-way ANOVA, Sidak's multiple comparisons test, Stim. versus Contra, $P = 0.0044$; Stim. versus Distal, $P = 0.0013$). Right bottom: summary of *tdT*$^-$*fos*$^+$ neurons (Stim., 30.00 ± 5.228; Contra, 7.5 ± 2.901; Distal, 3.0 ± 1.081; one-way ANOVA, Sidak's multiple comparisons test, Stim. versus Contra, $P = 0.0028$; Stim. versus Distal, $P = 0.0008$). Data are presented as mean ± s.e.m., $n = 4$ animals. **f**, Schematic of the in vivo extracellular electrophysiology recording setup using an MEA, with the µ-ILED positioned at varying distances along the cranial surface and operated at different optical power levels. **g**, Spatial distribution of electrodes on the MEA, with representative waveforms from a subset of units for one recording session. Scale bar, 250 µm. **h**, Raster plot showing spike activity of all single units before and after optogenetic stimulation from a µ-ILED adjacent to the MEA (stimulation, 4 Hz, 2-ms pulse width). **i**, Summary of the mean firing rate of all single units before and in a 2-ms time window immediately after optogenetic stimulation at different optical power levels. Data are presented as mean ± s.e.m. **j**, Histogram of unit distribution across firing rate bins before and after optogenetic stimulation. Inset: cumulative probability of firing rate distributions before stimulation and after stimulation. **k**, Summary of the mean firing rate of all single units before and in a 2-ms time window immediately after optogenetic stimulation at different distances to the center of µ-ILED at 6.49 mW optical power. Dots represent individual units; lines indicate mean ± s.e.m. Two-way ANOVA, Sidak's multiple comparisons test, Pre-stim. versus Post-stim., 419 µm, $P < 0.0001$, $n = 167$ units; 548 µm, $P < 0.0001$, $n = 172$ units; 613 µm, $P < 0.0001$, $n = 73$ units; 708 µm, $P < 0.0001$, $n = 62$ units; 909 µm, $P = 0.0005$, $n = 76$ units; 975 µm, $P < 0.0001$, $n = 67$ units; 1,206 µm, $P = 0.8260$, $n = 59$ units; 1,257 µm, $P = 0.8388$, $n = 68$ units; 1,505 µm, $P = 0.1633$, $n = 68$ units; 1,546 µm, $P = 0.1356$, $n = 65$ units. $^{**}P < 0.01$, $^{***}P < 0.001$, $^{****}P < 0.0001$. NS, not significant.

https://doi.org/10.1038/s41593-025-02127-6

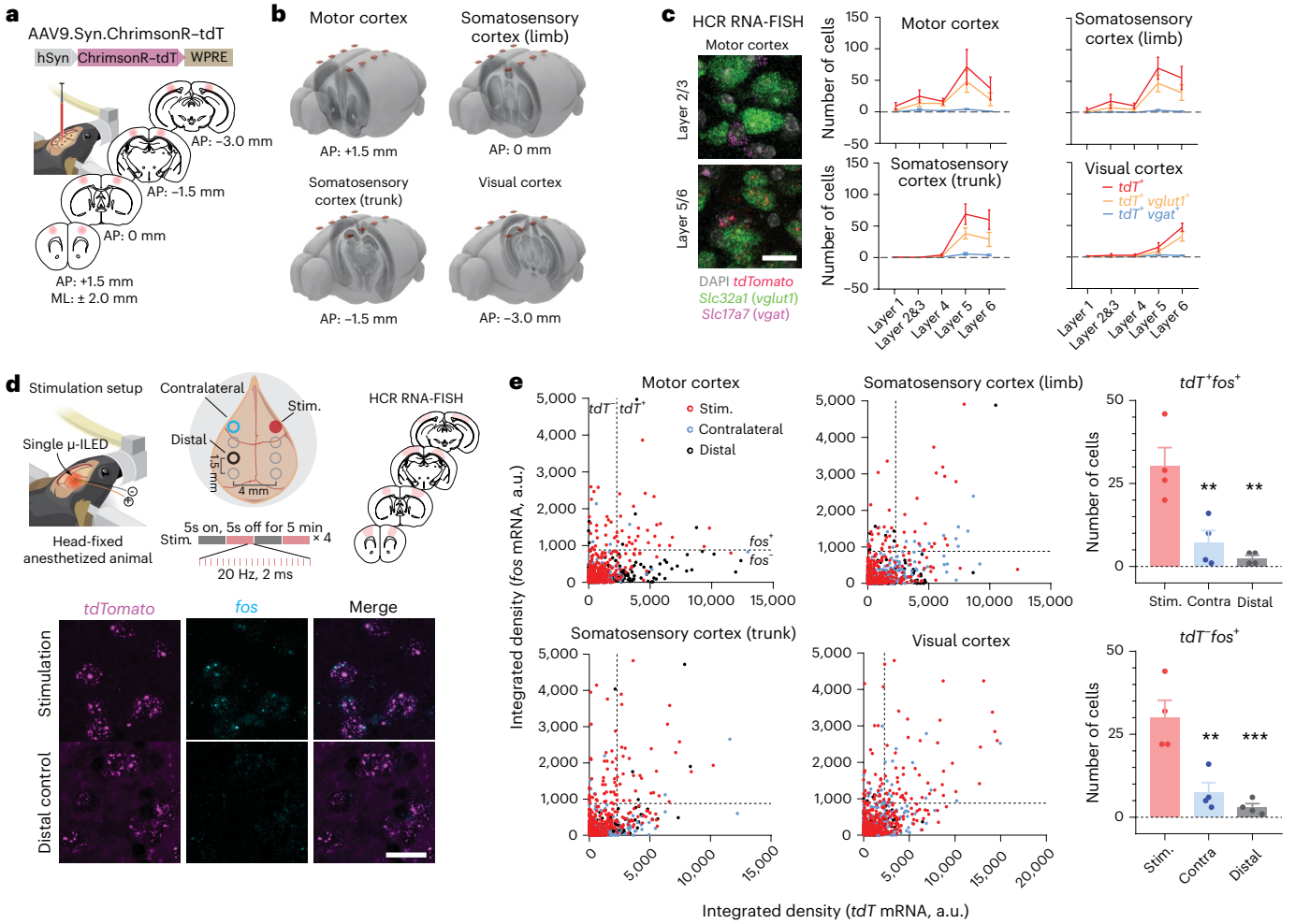

https://doi.org/10.1038/s41593-025-02127-6

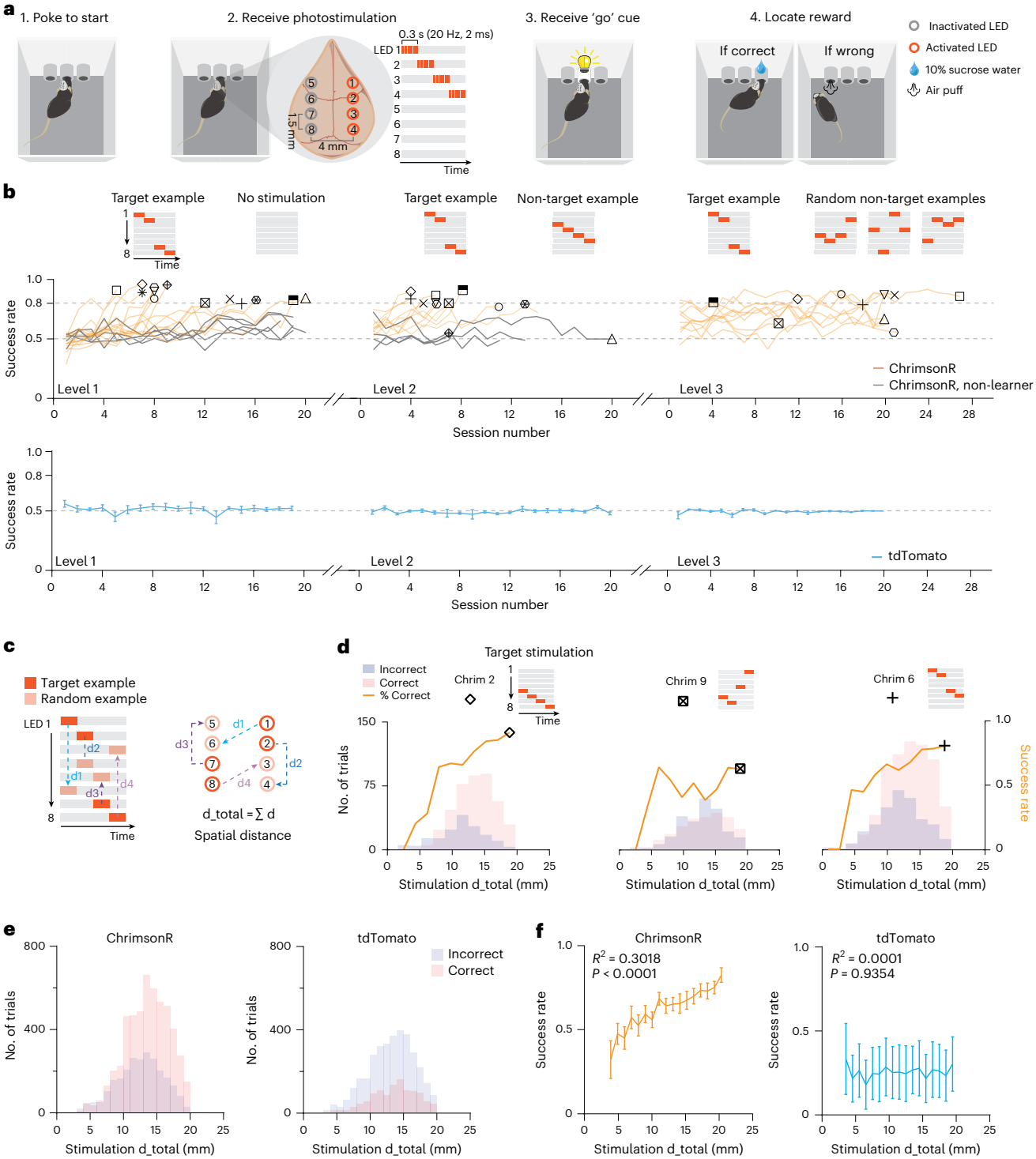

Fig. 4 | Sequential cortical activation drives operant learning based on cue discrimination. a, Schematic illustration of the operant learning task with artificial optogenetic cues. Mice make decisions based on the discrimination of cortical activation sequences, with successful trials rewarded by sucrose. **b**, Summary data showing the performance trajectories of cue discrimination for animals expressing ChrimsonR or tdTomato based on the success rate of obtaining sucrose rewards. Level 1, distinction of target sequence versus no stimulation; level 2, target sequence versus a certain non-target sequence; level 3, target sequence versus a pool of randomized sequences. Chance = 0.5. n = 15 animals for ChrimsonR and n = 5 animals for tdTomato. Each session includes up to 100 trials. Shapes and orange lines indicate individual animals that reached 80% success rate in level 1 (learners). Black lines indicate animals that failed to reach 80% success rate in level 1 (non-learners). Data of tdTomato controls are presented as mean ± s.e.m. **c**, Definition of spatial distance between the target sequence and individual randomized non-target sequence in level 3. **d**, Line plot showing success rate as a function of spatial distance for three individual animals in the level 3 task. The number of trials with correct or incorrect choices in each bin of spatial distance was plotted in the histogram. **e**, Summary data showing the number of trials with correct or incorrect choices in each bin of spatial distance from all animals expressing ChrimsonR or tdTomato. n = 10 animals for ChrimsonR and n = 5 animals for tdTomato. **f**, Summary data showing success rate as a function of spatial distance for all animals expressing ChrimsonR or tdTomato. n = 10 animals for ChrimsonR and n = 5 animals for tdTomato. ChrimsonR, one-way ANOVA, $F_{16,153}$ = 5.028, P < 0.0001; test for linear trend, R^2 (effect size) = 0.3018, P < 0.0001. tdTomato, one-way ANOVA, $F_{16,68}$ = 0.04772, P > 0.9999; test for linear trend, R^2 (effect size) = 0.0001, P = 0.9354. Data are presented as mean ± s.e.m.

https://doi.org/10.1038/s41593-025-02127-6

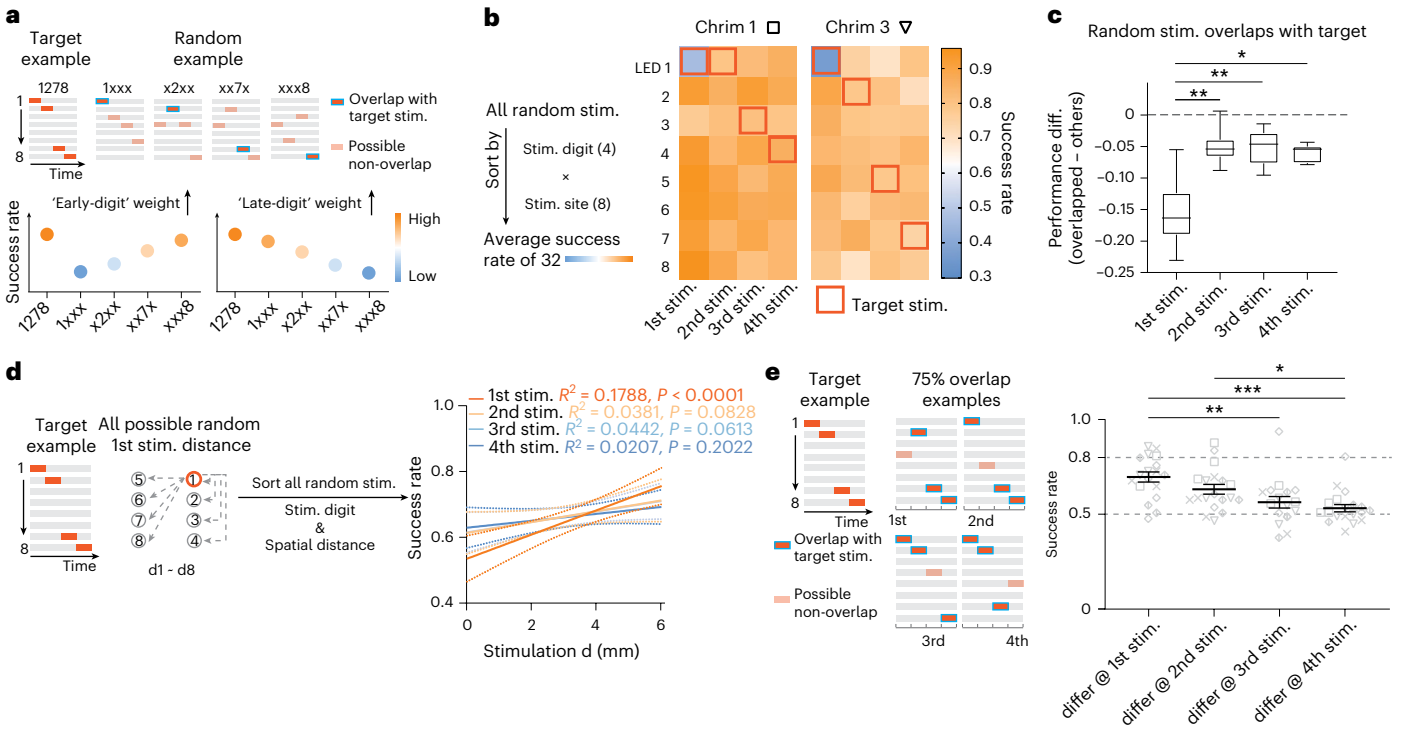

Fig. 5 | Temporal weighting in stimulus sequence modulates discrimination of spatially patterned activation. a, Hypothesized outcomes in the discrimination of sequential cortical activation based on the weighting of early or late stimulation digits. **b**, Left: schematic showing random non-target stimulation sorting based on the stimulation site (LED 1–8) and digits (1st–4th stim.). The color of each square is the average success rate for all patterns that include that square. Right: examples of non-target stimulation sorting in ChrimsonR-expressing animals; red squares indicate the target stimulation sequence for each animal. **c**, Summary data showing average performance change when randomized stimulation sequence overlaps with the target stimulation on each digit. 1st stim. (random stimulation overlaps with target on 1st digit), −0.1545 ± 0.0186; 2nd stim., −0.04981 ± 0.0097; 3rd stim., −0.0513 ± 0.0102; 4th stim., −0.0604 ± 0.0500. One-way ANOVA, $F_{2.046,14.32} = 11.43$, $P = 0.0010$, Sidak's multiple comparisons test, 1st versus 2nd stim., $P = 0.0038$; 1st versus 3rd stim., $P = 0.0071$; 1st versus 4th stim., $P = 0.0159$; 2nd versus 3rd stim., $P > 0.9999$; 2nd versus 4th stim., $P = 0.8221$; 3rd versus 4th stim., $P = 0.9171$. Box plots show the median (line), 25th and 75th percentiles (bounds of box) and minimum and maximum values (whiskers). $n = 10$ animals. **d**, Left: schematic illustration of non-target stimulation sorting based on the spatial distance from the target stimulation at each stimulation digit. Right: Pearson's correlation analysis of spatial distance and success rate based on stimulation digit. **e**, Experimental validation of the digit-weight effect in perception. Left: schematic illustration of experimental design. A group of probing sequences with 75% similarity (three stimulation digits) to the target sequences were used as non-target stimulations. Varying stimulation locations were selected at each non-overlapping digit for each animal. Right: summary data showing success rate in the 75% similarity probing tasks for each non-overlapping digit. Each data point represents a single 100-trial session, and each shape represents the animal used in Figs. 4 and 5. One-way ANOVA, $P < 0.0001$, $F_{3,69} = 8.327$, Sidak's multiple comparisons, 1st stim. versus 3rd stim., $P = 0.0030$, 1st stim. versus 4th stim., $P = 0.0001$, 2nd stim. versus 4th stim., $P = 0.0308$; differ @ 1st stim., $n = 18$ sessions; differ @ 2nd stim., $n = 19$ sessions; differ @ 3rd stim., $n = 17$ sessions; differ @ 4th stim., $n = 19$ sessions, from five animals.

optical power. Recordings in ChrimsonR$^-$ animals at varying distances captured stimulation artifacts associated with current delivery to the μ-ILED (Extended Data Fig. 7a,b). For both ChrimsonR$^+$ and ChrimsonR$^-$ animals, common-mode artifacts were estimated and removed using a version of the sequential principal components regression algorithm[29] (ERAASR; see Methods for details). In addition, local field potentials (LFPs) evoked by μ-ILED stimulation at varying input irradiances and distances are described in Extended Data Fig. 7c–f.

Sequential cortical activation drives operant learning based on cue discrimination

To address the feasibility of generating artificial perception through digitized optogenetic inputs, we employed an operant conditioning behavioral paradigm, where animals learn to identify artificial cues and respond to receive rewards[14,19,30]. We systematically manipulated neuronal activity in different cortical regions and quantitatively measured perceptual responses in decision-making tasks. As a proof of concept, we fabricated devices with 2 × 4 FOD configuration to target the motor cortex, somatosensory cortex spanning the limb regions, somatosensory cortex covering the trunk representation and the visual cortex in both hemispheres. The efficacy of transcranial optogenetic activation was visually confirmed by tonic motor responses elicited by prolonged high-frequency (20-Hz) light stimulation at the motor cortex, as described in our previous reports[9,11]. In the operant conditioning paradigm, mice initiated trials by nose-poking the center port. Subsequently, sequential cortical optogenetic inputs were delivered to four designated locations among the eight, each stimulated for 0.3 seconds at 20 Hz (six pulses at 6.12-mW optical power, with 2-ms pulse width). After stimulation termination, mice received a 'go' cue indicating that they could choose the left-side or the right-side port. If mice selected the port associated with the stimulation pattern, they received a sucrose reward droplet, whereas incorrect choices led to an air puff punishment (Fig. 4a).

We trained mice to discriminate a designated target sequence in three tasks of progressive difficulty. The simplest task required discrimination against null stimulation, where none of the LEDs lit up. After achieving a high success rate (80%), mice had to discriminate the target sequence against a specific non-target sequence. After pretraining on level 1 and level 2 tasks, mice received a pool of randomly generated non-target sequences in the trials, requiring discrimination of the target sequence from this pool (Fig. 4b). A subset of ChrimsonR-expressing mice learned to reach higher success rates across the three levels of

tasks within 10 days (median number of sessions: eight for level 1; five for level 2; 14 for level 3) (Extended Data Fig. 8a,b), whereas the performance of tdTomato-expressing control mice remained at chance level (0.5) after 20 sessions at each task level (Fig. 4b).

Because of non-uniform connectivity across the broader cortical space[31–33], it was unknown whether a larger physical distance between stimulation locations correlated strongly with stimulus discriminability. We, therefore, utilized the randomized non-target sequences from the level 3 task to construct a spatial distance framework correlating sequence discrimination performance with spatial distance on the cortical map (Fig. 4c). Distinct distributions of success and failure trials based on the spatial distance of the randomized sequence were observed in the data collected from individual animals. Success rate increased as the non-target sequence spatial distance from the designated target sequence increased (Fig. 4d). The distribution of trial outcomes and the trends in success rate persisted at the group level. By contrast, trial outcomes from tdTomato-expressing controls were not associated with the spatial distance of sequences (Fig. 4e,f). These findings suggest that spatial distance among sequential cortical activations contributes to the discriminability of spatiotemporally patterned artificial stimuli provided by the FOD. Before and after postoperative recovery from device implantation, mice displayed no significant changes in velocity, acceleration and exploration of the environment during open field locomotion (Extended Data Fig. 8c,d). These findings confirm that our miniaturized wireless systems minimally perturb natural movement. Analyses of reaction times show a similar distribution for correct and incorrect behavioral outcomes (Extended Data Fig. 8e,f). Individual-level behavioral analyses depict the variability of responses within and across animals (Extended Data Fig. 9).

Temporal weighting modulates discrimination of spatially patterned activation

Next, we examined whether the earlier stimuli in a pattern influence behavior in the same ways as the later ones. For this experiment, we treat the temporal order of each stimulation location (the 'digits' of the sequence) as an independent variable. Randomly generated non-target patterns are categorized based on stimulated cortical locations for each digit. For example, non-target stimulation trials initiated with motor cortex stimulation were grouped, and the total success rate for these trials was calculated (Fig. 5a). We hypothesized that the contribution of each digit to perceptual discrimination may vary based on placement in the temporal sequence, analogous to the temporal weighting framework from perceptual psychology[34–37]. This framework, applied to the current experiment, predicts that performance will be worse when there is overlap between target and non-target stimuli at the digits more heavily weighted by the subjects. For example, if earlier activations are assigned greater weight, then overlap early in the sequence would have a stronger negative impact on performance, whereas greater weighting of later activations would result in worse performance when digit overlap occurs later in the sequence (Fig. 5a).

Our results demonstrate that overlapping stimulated cortical regions between target and non-target sequences at the first digit result in the lowest success rate, consistent with heavier weights assigned to early incoming stimuli (Fig. 5b and Extended Data Fig. 9b). Furthermore, overlap between target and random stimuli in the first digit place had a greater negative impact on performance, compared to overlap in digits 2–4 (Fig. 5c). Additionally, temporal sequence modulated spatial distance effects on perceptual discrimination as follows. We observed a stronger correlation between spatial distance and success rate for the first digit in the stimulation compared to later ones (Fig. 5d and Extended Data Fig. 9c). In other words, spatial distance in the first digit of a stimulation sequence helped perceptual discrimination of target versus non-target stimuli more than spatial distance between subsequent digits.

To further explore the temporal weighting of different digits revealed in the previous experiments with random non-targets, we next tested mice on discriminating non-random stimulation sequences with high overlap with the learned target sequence (50–75%). After the three levels of learning (Fig. 4), mice were presented with a group of probing non-target sequences that were similar to the target sequences (50–75% similarity—that is, 2–3 overlapping digits). Mice performed significantly better at distinguishing 50% similarity sequences compared to 75% (Extended Data Fig. 10a). In the 75% similarity probing task, we further test the temporal weighting of digits 1–4 by varying the non-overlapping stimulation digit (Fig. 5e). Consistent with our previous observations, mice performed better when the non-overlapping digit came earlier (digits 1–2) rather than later (digits 3–4) in the sequence. We also carried out a series of additional cue discrimination experiments exploring parts of the very large available stimulation parameter space in the current FOD. These include discrimination of stimuli of varying durations at single sites, discrimination of neighboring single-site stimulations within or across hemispheres as well as discrimination of the same set of stimulation sites with reversed order (Extended Data Fig. 10b–h and Supplementary Table 4). Our results demonstrate that mice are able to discriminate cues across diverse sets of parameters of patterned stimulation from the FOD. Some combinations of stimulation parameters are easier for the mice to learn than others, and aspects of their performance can be predicted by relevant studies from psychology[34,35,38,39].

Discussion

In this study, we developed a fully implantable optogenetic neural interface and a supporting ecosystem of technologies for wireless transmission of digitized information to a large-scale network of neurons. The reported device uses an array of individually addressable optical stimulators to transcranially deliver spatiotemporally programmable patterns of illumination to targeted cortical areas. Real-time programmability of location, time and stimulation intensity provides multiple degrees of freedom, enabling dynamic modulation of cortex-wide activity. The mechanically compliant, fully subdermally implantable form factor allows its usage in freely moving animals without external physical constraints, facilitating the study of artificial perception delivery within behavioral contexts. Furthermore, experimentally validated comprehensive numerical simulations on transcranial light penetration and thermal dissipation profiles, along with the characterization of neuronal activity evoked by transcranial patterned optogenetic stimulation, serve as detailed guidance for future technology designs for neuroscience applications. We expect that this robust and scalable platform is generalizable to accommodate various applications and animal models.

Key technological innovations

Our fully implantable device, equipped with individually addressable μ-ILEDs on a configurable FOD, offers a wireless alternative to existing head-fixed approaches using microscopy or dense fiber bundles. Its wireless capability facilitates the investigation of mesoscale cortex-wide neural dynamics in untethered, freely moving animals. The current studies, beyond providing proof-of-principle experiments for the current FOD, also elaborate the contexts for perception of artificially patterned cortical activity in freely moving and freely learning mice. Many types of behavioral and systems neuroscience experiments may benefit by the technology we introduce, although it is not suitable for subcortical stimulation, for fine-scale spatial mapping or for targeting single neurons or very small neuronal groups. Well-aligned experimental paradigms include transcranial patterned control of neuromodulatory systems that have broad axonal distribution in the cortex (for example, dopamine, acetylcholine and serotonin). Moreover, in combination with advanced genetic targeting strategies, cell-type-specific promoters, subcellular targeting and sparse labeling, this technology enables controlled manipulation of specific cortical layers, cell populations or projection-specific ensembles[40–44]. With this

wireless, small, programmable device, it is possible to implement the above in ways that are conditional on complex behaviors, including social interactions in groups of animals, multistep learning assays and extended experiments with freely moving animals.

Some of the transformative potential of this technology lies in its adaptability and scalability. We have already demonstrated scalability by increasing the density of μ-ILEDs from 2 × 4 to configurations such as 4 × 7 and 8 × 8 arrays, with minor modifications to the device form factor (Supplementary Videos 1 and 3). For any array size (such as 2 × 4 or 8 × 8) at the current μ-ILED size operating sequentially, the cumulative thermal load at any given brain location cannot exceed that of a single μ-ILED in continuous operation directly above it, which we have simulated and measured, establishing a ceiling temperature rise (<0.1 °C at the brain surface (Fig. 2h–k)). Given that temperature rise scales linearly with input power, the same thermal and FEA models can be used to estimate heating for a range of stimulation intensities and configurations. Additionally, experimental temperature measurements from Extended Data Fig. 5 may be used to approximate heating profiles under other combinations of frequencies and duty cycles. However, the 8 × 8 arrays have not yet been evaluated at the level of behavioral assays. Given the potential for co-activation of the same neuron from multiple stimulation sites at higher density of μ-ILEDs, perceptual discriminability of varied 8 × 8 patterns will need to be validated in future behavioral experiments. For broad adaptability, μ-ILEDs of different wavelengths can be combined into a single FOD, whether the goal is to stimulate the same approximate regions with different wavelength stimuli or to target two distal parts of the cortex with different opsins. This concept was recently demonstrated with three LEDs at red and near-infrared wavelengths to bilaterally stimulate premotor cortex and unilaterally activate the superior colliculus[45]. Likewise, emerging variants of new light-sensitive proteins[46], together with multi-wavelength FOD, may facilitate experiments requiring dynamic neuronal activation, inhibition or modulation across cortical regions. The scalability and adaptability of this platform are increased by the accessibility and low cost of its materials, which are easily obtainable through institutional core facilities or commercially available PCBs and device turnkey services. To encourage widespread adoption, we have provided fabrication steps (Extended Data Fig. 1), component lists, designs and models ('Data availability' and 'Code availability'), ensuring that neuroscience laboratories worldwide can implement this technology in their research.

Compared to existing approaches, our system offers a balance of accessibility and functionality. Although two-photon holography optogenetics provides unparalleled precision in targeting specific neuronal ensembles or, in some cases, even individual neurons[12–14,19], it requires complex and costly optical systems. Furthermore, reliance on head fixation limits its utility for studying some naturalistic and multi-agent behaviors. In a complementary way, our approach facilitates mesoscale, minimally invasive transcranial modulation in freely moving animals, expanding the toolkit for systems and behavioral neuroscience with a cost-effective, versatile platform for manipulating large-scale cortical dynamics compatible with naturalistic, environmentally enriched paradigms.

Perceptual discrimination of artificial cortical activation

Using the technology advanced in this paper, we constructed a framework to investigate perceptual responses to patterned artificial cortical activation. By measuring discrimination-based perceptual responses to systematic and randomized input manipulations, we adapted approaches inspired by psychological studies in humans and animals aiming to explore principles underlying artificial perception[14,19,47]. Our findings demonstrate that perceptual discrimination is influenced by the spatial similarity of patterned cortical activation, further modulated by the temporal order of stimulation sites.

The role of sensory modalities and cortical architecture in perceptual discrimination and learning is well recognized[48–51]. Stimulating distinct cortical regions associated with sensory and motor functions elicits different perceptual and behavioral outcomes, further complicating the analyses of artificially patterned cortical activation. Our behavioral analyses revealed significant differences in learning efficacy based on the spatial and hemispheric origins of cortical stimulation. Animals display higher success rates when discriminating against same-modality stimulations across hemispheres compared to within-hemisphere, cross-modality activation (two-sided unpaired *t*-test, ipsilateral versus contralateral, $P = 0.0053$; Extended Data Fig. 10c–e). Additionally, potential differences in behavioral responses to stimulation of sensory versus motor cortices may relate to how animals interpret these activations. For example, early-in-sequence stimulation of motor cortices, potentially reducing the activation threshold to action, could elicit more robust learning outcomes compared to patterns that initiate in sensory cortices. Alternatively, motor commands may recruit peripheral mechanoreceptors that amplify the associated somatosensory percepts to enhance discriminability[52,53]. Even with a necessarily limited sample size, our present study reveals both individual variability in the learning of artificial cortical stimulation patterns and stimulus structure-related regularities that can be used to probe questions about multimodal integration of cortical activity and broader systems neuroscience themes.

Temporal order further emerges as a factor regulating the discrimination of artificially induced cortical activation patterns. Temporal variables in sensory events are well known to modulate a range of natural perceptual processes across tactile, auditory and visual domains[38,39,54,55]. To isolate the effects of temporal order, we constrain other temporal variables, such as stimulation duration, number of pulses and inter-stimulus intervals, allowing temporal order of stimulation sites alone to drive perceptual differences. Our analyses reveal that earlier time intervals are weighted more heavily in discrimination tasks, consistent with psychological studies demonstrating the disproportionate influence of early stimuli on perceptual decisions[36,37]. Although this finding aligns with potential serial position effects, we caution against direct generalization to established psychological principles due to the fundamental differences between naturalistic sensory inputs and artificially patterned activations. Future studies could leverage systematic variations in temporal intervals to disentangle biases in temporal order processing from effects specific to the timing of artificial stimuli. Such investigations, well supported by the current device capabilities, could yield deeper insights into the interactions between temporal variables and perceptual discrimination in artificial cortical activation.

Potential applications in BMI and bio-inspired robotics

The wireless, battery-free and completely subdermal nature of this device reduces the cleaning and maintenance requirements for a potential prosthesis when compared with current BMI stimulation methods[3]. Additionally, the transcranial FOD is less invasive, and a fully wireless, subcutaneous control module allows greater mobility. Recent studies relying on electrical intracortical microstimulation (ICMS) in human patients with spinal cord injury have shown that stimulating overlapping projected fields within the cutaneous areas of primary somatosensory cortex allows for greater localization and intensity of sensation[56]. The adjustability of the FOD form factor, as well as the location and density of LEDs, may allow researchers to work with the patients to create stimuli sets that are more discriminable than current ICMS methods. The FOD would also be able to cover a larger area than a single MEA and could potentially stimulate more discriminable percepts[6]. As optogenetic tools for human application continue to advance[57,58], the combination of targeted opsin expression and wireless patterned stimulation will support new modes of neural activity control over subpopulations. By enabling programmable flexible activation patterns, this platform could provide a valuable tool for next-generation neuroprosthetic systems.

Future technical development

Future development of this device platform can focus on enhancing the spatial resolution of optogenetic stimulation. This goal can be achieved by increasing the number and reducing the size of optogenetic stimulators, leveraging advancements in semiconductor technology or microfabricated μ-ILEDs. Digital control methods offer a promising approach to address multiple optoelectronic components with minimal wiring, enabling complex stimulation patterns while maintaining a compact device footprint[59]. Additionally, transferring the stimulator arrays onto compliant substrates will extend their applications to peripheral nervous systems and other organs, further driving innovation in neural interface technology. The soft, minimally invasive nature of this future interface also enhances its translational potential, particularly for therapeutic applications in non-human primates and humans. Opsin-independent photomodulation presents another exciting avenue for clinical translation of this technology, bypassing the need to introduce genetic modifications for certain applications[60].

In its current design, the device platform does not support real-time neural recording capabilities or closed-loop control mechanisms. Introducing advanced electronic modules capable of bidirectional communication, such as those using Bluetooth low energy (BLE) or Wi-Fi[24], could support simultaneous neural recording and optogenetic stimulation in a closed-loop configuration. The platform's adaptability and compatibility with open-source platforms in behavioral neuroscience, including autonomous behavioral training systems[61], offer substantial opportunities for high-throughput experimental studies. Future development of this technology could incorporate further improvements to enable sustained operation in biological systems.

Online content

Any methods, additional references, Nature Portfolio reporting summaries, source data, extended data, supplementary information, acknowledgements, peer review information; details of author contributions and competing interests; and statements of data and code availability are available at https://doi.org/10.1038/s41593-025-02127-6.

References

1. Lebedev, M. A. & Nicolelis, M. A. L. Brain–machine interfaces: past, present and future. *Trends Neurosci.* **29**, 536–546 (2006).
2. Serino, A. et al. Sense of agency for intracortical brain–machine interfaces. *Nat. Hum. Behav.* **6**, 565–578 (2022).
3. Tang, X., Shen, H., Zhao, S., Li, N. & Liu, J. Flexible brain–computer interfaces. *Nat. Electron* **6**, 109–118 (2023).
4. O'Doherty, J. E. et al. Active tactile exploration using a brain–machine–brain interface. *Nature* **479**, 228–231 (2011).
5. Flesher, S. N. et al. A brain-computer interface that evokes tactile sensations improves robotic arm control. *Science* **372**, 831–836 (2021).
6. Rapeaux, A. B. & Constandinou, T. G. Implantable brain machine interfaces: first-in-human studies, technology challenges and trends. *Curr. Opin. Biotechnol.* **72**, 102–111 (2021).
7. Shin, G. et al. Flexible near-field wireless optoelectronics as subdermal implants for broad applications in optogenetics. *Neuron* **93**, 509–521 (2017).
8. Yang, Y. et al. Wireless multilateral devices for optogenetic studies of individual and social behaviors. *Nat. Neurosci.* **24**, 1035–1045 (2021).
9. Ausra, J. et al. Wireless, battery-free, subdermally implantable platforms for transcranial and long-range optogenetics in freely moving animals. *Proc. Natl Acad. Sci. USA* **118**, e2025775118 (2021).
10. Yang, Y. et al. Preparation and use of wireless reprogrammable multilateral optogenetic devices for behavioral neuroscience. *Nat. Protoc.* **17**, 1073–1096 (2022).
11. Wu, Y. et al. Wireless multi-lateral optofluidic microsystems for real-time programmable optogenetics and photopharmacology. *Nat. Commun.* **13**, 5571 (2022).
12. Marshel, J. H. et al. Cortical layer–specific critical dynamics triggering perception. *Science* **365**, eaaw5202 (2019).
13. Robinson, N. T. M. et al. Targeted activation of hippocampal place cells drives memory-guided spatial behavior. *Cell* **183**, 1586–1599 (2020).
14. Gill, J. V. et al. Precise holographic manipulation of olfactory circuits reveals coding features determining perceptual detection. *Neuron* **108**, 382–393 (2020).
15. Carrillo-Reid, L., Han, S., Yang, W., Akrouh, A. & Yuste, R. Controlling visually guided behavior by holographic recalling of cortical ensembles. *Cell* **178**, 447–457 (2019).
16. Oldenburg, I. A. et al. The logic of recurrent circuits in the primary visual cortex. *Nat. Neurosci.* **27**, 137–147 (2024).
17. Adesnik, H. & Abdeladim, L. Probing neural codes with two-photon holographic optogenetics. *Nat. Neurosci.* **24**, 1356–1366 (2021).
18. Bollmann, Y. et al. Prominent in vivo influence of single interneurons in the developing barrel cortex. *Nat. Neurosci.* **26**, 1555–1565 (2023).
19. Chong, E. et al. Manipulating synthetic optogenetic odors reveals the coding logic of olfactory perception. *Science* **368**, eaba2357 (2020).
20. Pinto, L. & Dan, Y. Cell-type-specific activity in prefrontal cortex during goal-directed behavior. *Neuron* **87**, 437–450 (2015).
21. Pinto, L. et al. Task-dependent changes in the large-scale dynamics and necessity of cortical regions. *Neuron* **104**, 810–824 (2019).
22. Pinto, L., Tank, D. W. & Brody, C. D. Multiple timescales of sensory-evidence accumulation across the dorsal cortex. *eLife* **11**, e70263 (2022).
23. Cox, J. & Witten, I. B. Striatal circuits for reward learning and decision-making. *Nat. Rev. Neurosci.* **20**, 482–494 (2019).
24. Ouyang, W. et al. A wireless and battery-less implant for multimodal closed-loop neuromodulation in small animals. *Nat. Biomed. Eng.* **7**, 1252–1269 (2023).
25. Stujenske, J. M., Spellman, T. & Gordon, J. A. Modeling the spatiotemporal dynamics of light and heat propagation for in vivo optogenetics. *Cell Rep.* **12**, 525–534 (2015).
26. Owen, S. F., Liu, M. H. & Kreitzer, A. C. Thermal constraints on in vivo optogenetic manipulations. *Nat. Neurosci.* **22**, 1061–1065 (2019).
27. Wang, Q. et al. The Allen Mouse Brain Common Coordinate Framework: a 3D reference atlas. *Cell* **181**, 936–953 (2020).
28. Klapoetke, N. C. et al. Independent optical excitation of distinct neural populations. *Nat. Methods* **11**, 338–346 (2014).
29. O'Shea, D. J. & Shenoy, K. V. ERAASR: an algorithm for removing electrical stimulation artifacts from multielectrode array recordings. *J. Neural Eng.* **15**, 026020 (2018).
30. Nakayama, H., Gerkin, R. C. & Rinberg, D. A behavioral paradigm for measuring perceptual distances in mice. *Cell Rep. Methods* **2**, 100233 (2022).
31. Harris, K. D. & Mrsic-Flogel, T. D. Cortical connectivity and sensory coding. *Nature* **503**, 51–58 (2013).
32. Leech, R. et al. Variation in spatial dependencies across the cortical mantle discriminates the functional behaviour of primary and association cortex. *Nat. Commun.* **14**, 5656 (2023).
33. Paolino, A. et al. Non-uniform temporal scaling of developmental processes in the mammalian cortex. *Nat. Commun.* **14**, 5950 (2023).
34. Levi, A. J., Yates, J. L., Huk, A. C. & Katz, L. N. Strategic and dynamic temporal weighting for perceptual decisions in humans and macaques. *eNeuro* **5**, ENEURO.0169–18.2018 (2018).
35. Hyafil, A. et al. Temporal integration is a robust feature of perceptual decisions. *eLife* **12**, e84045 (2023).

36. Resulaj, A., Ruediger, S., Olsen, S. R. & Scanziani, M. First spikes in visual cortex enable perceptual discrimination. *eLife* **7**, e34044 (2018).
37. Nienborg, H. & Cumming, B. G. Decision-related activity in sensory neurons reflects more than a neuron's causal effect. *Nature* **459**, 89–92 (2009).
38. Weber, A. I. et al. Spatial and temporal codes mediate the tactile perception of natural textures. *Proc. Natl Acad. Sci. USA* **110**, 17107–17112 (2013).
39. Gavornik, J. P. & Bear, M. F. Learned spatiotemporal sequence recognition and prediction in primary visual cortex. *Nat. Neurosci.* **17**, 732–737 (2014).
40. Baker, C. A., Elyada, Y. M., Parra, A. & Bolton, M. M. Cellular resolution circuit mapping with temporal-focused excitation of soma-targeted channelrhodopsin. *eLife* **5**, e14193 (2016).
41. Daigle, T. L. et al. A suite of transgenic driver and reporter mouse lines with enhanced brain-cell-type targeting and functionality. *Cell* **174**, 465–480 (2018).
42. Sridharan, S. et al. High-performance microbial opsins for spatially and temporally precise perturbations of large neuronal networks. *Neuron* **110**, 1139–1155 (2022).
43. Kim, C. K., Adhikari, A. & Deisseroth, K. Integration of optogenetics with complementary methodologies in systems neuroscience. *Nat. Rev. Neurosci.* **18**, 222–235 (2017).
44. Ben-Simon, Y. et al. A suite of enhancer AAVs and transgenic mouse lines for genetic access to cortical cell types. *Cell* **188**, 3045–3064 (2025).
45. Shin, H. et al. Transcranial optogenetic brain modulator for precise bimodal neuromodulation in multiple brain regions. *Nat. Commun.* **15**, 10423 (2024).
46. McCue, A. C. & Kuhlman, B. Design and engineering of light-sensitive protein switches. *Curr. Opin. Struct. Biol.* **74**, 102377 (2022).
47. Duncan, J. Selective attention and the organization of visual information. *J. Exp. Psychol. Gen.* **113**, 501–517 (1984).
48. Lemus, L., Hernández, A., Luna, R., Zainos, A. & Romo, R. Do sensory cortices process more than one sensory modality during perceptual judgments? *Neuron* **67**, 335–348 (2010).
49. O'Riordan, M. & Passetti, F. Discrimination in autism within different sensory modalities. *J. Autism Dev. Disord.* **36**, 665–675 (2006).
50. Mondor, T. A. & Amirault, K. J. Effect of same- and different-modality spatial cues on auditory and visual target identification. *J. Exp. Psychol. Hum. Percept. Perform.* **24**, 745–755 (1998).
51. Karlin, L. & Mortimer, R. G. Effect of verbal, visual, and auditory augmenting cues on learning a complex motor skill. *J. Exp. Psychol.* **65**, 75–79 (1963).
52. Niyo, G., Almofeez, L. I., Erwin, A. & Valero-Cuevas, F. J. A computational study of how an α- to γ-motoneurone collateral can mitigate velocity-dependent stretch reflexes during voluntary movement. *Proc. Natl Acad. Sci. USA* **121**, e2321659121 (2024).
53. Berry, J. A., Marjaninejad, A. & Valero-Cuevas, F. J. Edge computing in nature: minimal pre-processing of multi-muscle ensembles of spindle signals improves discriminability of limb movements. *Front. Physiol.* **14**, 1183492 (2023).
54. Cascio, C. J. & Sathian, K. Temporal cues contribute to tactile perception of roughness. *J. Neurosci.* **21**, 5289–5296 (2001).
55. Hirsh, I. J. Auditory perception of temporal order. *J. Acoust. Soc. Am.* **31**, 759–767 (1959).
56. Greenspon, C. M., Shelchkova, N. D., Hobbs, T. G., Bensmaia, S. J. & Gaunt, R. A. Intracortical microstimulation of human somatosensory cortex induces natural perceptual biases. *Brain Stimul.* **17**, 1178–1185 (2024).
57. Sahel, J.-A. et al. Partial recovery of visual function in a blind patient after optogenetic therapy. *Nat. Med.* **27**, 1223–1229 (2021).
58. Drew, L. Restoring vision with optogenetics. *Nature* **639**, S7–S9 (2025).
59. Taal, A. J. et al. Optogenetic stimulation probes with single-neuron resolution based on organic LEDs monolithically integrated on CMOS. *Nat. Electron* **6**, 669–679 (2023).
60. Wang, Y., Garg, R., Cohen-Karni, D. & Cohen-Karni, T. Neural modulation with photothermally active nanomaterials. *Nat. Rev. Bioeng.* **1**, 193–207 (2023).
61. Saunders, J. L., Ott, L. A. & Wehr, M. AUTOPILOT: automating experiments with lots of Raspberry Pis. Preprint at *bioRxiv* https://doi.org/10.1101/807693 (2019).

[1]Querrey Simpson Institute for Bioelectronics, Northwestern University, Evanston, IL, USA. [2]Department of Neurobiology, Northwestern University, Evanston, IL, USA. [3]Department of Mechanical Engineering, Northwestern University, Evanston, IL, USA. [4]Department of Mechanical Engineering, Massachusetts Institute of Technology, Cambridge, MA, USA. [5]The N.1 Institute for Health, National University of Singapore, Singapore, Singapore. [6]Department of Biomedical Engineering, National University of Singapore, Singapore, Singapore. [7]Department of Biomedical Engineering, Northwestern University, Evanston, IL, USA. [8]Department of Civil and Environmental Engineering, Northwestern University, Evanston, IL, USA. [9]State Key Laboratory of Mechanical System and Vibration, School of Mechanical Engineering, Shanghai Jiao Tong University, Shanghai, China. [10]State Key Laboratory of Structural Analysis, Optimization and CAE Software for Industrial Equipment, Department of Engineering Mechanics, Dalian University of Technology, Dalian, China. [11]Department of Electrical and Computer Engineering, North Carolina State University, Raleigh, NC, USA. [12]Center for Advanced Self-Powered Systems of Integrated Sensors and Technologies (ASSIST), North Carolina State University, Raleigh, NC, USA. [13]Pritzker School of Molecular Engineering, The University of Chicago, Chicago, IL, USA. [14]Computation and Neural Systems, California Institute of Technology, Pasadena, CA, USA. [15]Department of Materials Science and Engineering, Northwestern University, Evanston, IL, USA. [16]Department of Biomedical Engineering and the Institute of Materials Science, University of Connecticut, Storrs, CT, USA. [17]Center for Bio-Integrated Electronics, Northwestern University, Evanston, IL, USA. [18]Neurolux, Inc., Northfield, IL, USA. [19]Department of Neuroscience, Feinberg School of Medicine, Northwestern University, Chicago, IL, USA. [20]Department of Neurobiology, The University of Chicago, Chicago, IL, USA. [21]Chemistry of Life Processes Institute, Northwestern University, Evanston, IL, USA. [22]Department of Neurological Surgery, Feinberg School of Medicine, Northwestern University, Chicago, IL, USA. [23]These authors contributed equally: Mingzheng Wu, Yiyuan Yang, Jinglan Zhang, Andrew I. Efimov, Xiuyuan Li, Kaiqing Zhang. ✉e-mail: yyy@nus.edu.sg; abraham.vg@ncsu.edu; y-huang@northwestern.edu; yevgenia.kozorovitskiy@northwestern.edu; jrogers@northwestern.edu

Methods

Device fabrication and assembly

A third-party vendor (PCBWay) produced the fPCB via laser ablation for the electronic module, the μ-ILED panel and the serpentine interconnect based on designs created using commercial computer-aided design (CAD) software (AutoCAD; Autodesk). The fPCB substrate for the electronic module and μ-ILED panel used a three-layer copper (18 μm)–polyimide (25 μm)–copper (18 μm) fPCB design. Alternatively, polyester (PET, 64 μm) may be used to replace polyimide to enhance the optical transparency of the devices. The fPCB substrate for the serpentine interconnect used a five-layer copper (12 μm)–polyimide (12.5 μm)–copper (12 μm)–polyimide (12.5 μm)–copper (12 μm) fPCB design. The total thickness was approximately 100/200 μm for polyimide/PET-based circuit boards with solder mask layers and approximately 60 μm for serpentine interconnects. Hot air soldering using a heat gun operated at 220–270 °C and low-temperature solder paste (Indium Corporation) electrically bonded the commercial electronic and optical components on the fPCB to establish the function of the electronic module and the μ-ILED panel. The same soldering strategy further electrically connected the electronic module and the μ-ILED panel with the serpentine trace to form the complete device. The chemical vapor deposition (CVD) process then formed a uniform parylene encapsulation coating (14 μm) around the device. Additional dip-coated epoxy (Norland 63) cured by ultraviolet light exposure mechanically secured and encapsulated the solder joints. Finally, mold-cast silicone coatings (Ecoflex 00-30, 400 μm) symmetrically covered the top and bottom surfaces of the serpentine trace and electronic module.

Smart NFC wireless electronic device

A 10-turn planar coil surrounding the perimeter of the device enabled magnetic inductive coupling to an external antenna for NFC and wireless power transfer. The harvested power was buffered on a five-22-μF ceramic capacitor bank that allowed storage of approximately 1.3 mJ of charge when completely charged (5 V). The harvested power was regulated with a 2.8-V low dropout regulator to provide constant voltage to the electronics. The NFC memory (STMicroelectronics, M24LR04E-R) provided standardized (ISO 15693) NFC communication with an external radiofrequency NFC driver (Neurolux, Inc., PDC Box) as the basis for bidirectional communication. A low-power 8-bit microcontroller (Microchip Technology, Inc., Attiny84) equipped with dedicated firmware received remote commands through the NFC memory and implemented spatiotemporal activation of the eight μ-ILEDs (Three-Five Materials, TCE12-628).

Hybrid analog/digital matrix multiplexing

The independent control of the eight μ-ILEDs is based on matrix multiplexing where two variable voltage lines connect the rows at the anodes of the μ-ILEDs and four digital lines connect to the columns at the cathodes (Extended Data Fig. 3). The use of two independently addressable digital-to-analog converters (DACs) connected with the microcontroller via I2C provides user-defined voltage levels. The use of the other four digital control lines allows for forward biasing only when writing logic 0 but not otherwise. This combination of hybrid analog/digital multiplexing serves as the basis for independent μ-ILED activation at programmable voltages.

This simple matrix intensity modulation approach requires only two DAC chips (2 mm × 2 mm each; Microchip Technology Inc., MCP4706). By contrast, other intensity control implementations increase the component count and complexity of the electronics, posing an integration challenge in the limited space available in the implantable device with dimensions compatible with mice. These alternative approaches include, on a per-channel basis, the Howland voltage-controlled current source (one operational amplifier chip and four passive resistive elements) and a voltage-controlled transconductance amplifier current source (one operational amplifier chip, one transistor and one resistor), where both cases also require the use of a voltage source such as the DACs.

Implementation of wirelessly programmable, intensity-controlled spatiotemporal illumination

The wireless device generates programmable spatiotemporal patterns of activation using the following approach. A read/write radiofrequency-accessible non-volatile memory (STMicroelectronics, M24LR04E-R) receives commands via NFC. This NFC memory, connected with the microcontroller (Microchip Technology, Inc., Attiny84) via I^2C, produces an interruption to the protocol upon command arrival. The microcontroller, prompted by this interruption, reads a memory block consisting of four bytes that contain the sequence/activation order for μ-ILEDs. Each byte includes the information for the μ-ILED index to activate (four least significant bits) and up to 16 intensity levels (four most significant bits). The channel selection and intensity are then sent to the analog/digital hybrid matrix multiplexer to forward bias to the selected μ-ILED at one of the 16 preprogrammed voltage levels. This block of memory is written via NFC on demand as required by the progression of the behavioral protocol. It is worth mentioning that the 16 preprogrammed voltages can be updated via NFC before the start of the experiment. Operational parameters, such as frequency and pulse widths per μ-ILED and delay between μ-ILEDs in the sequence, are also user defined via NFC. These values, once written, will remain in memory until further update, if necessary. This way, universal firmware can be used without the need for firmware customization per application.

Mechanical modeling and characterization

The commercial software Abaqus (Dassault Systèmes Simulia Corp. (2020)) was used to assess the mechanical characteristics of the device[62–65]. The circuit board, the FOD and the serpentine interconnect were modeled by composite shell elements (S4 elements), consisting of films of copper, polyimide and parylene. The Young's modulus and Poisson's ratio of the film materials are as follows: E_{Cu} = 130 GPa, ν_{Cu} = 0.34, E_{PI} = 2.5 GPa, ν_{PI} = 0.34, $E_{Parylene}$ = 2.1 GPa and $\nu_{Parylene}$ = 0.34 (ref. 8). All components were embedded in silicone (Ecoflex 00-30) encapsulation. The encapsulation was modeled using tetrahedron elements (C3D10H). Mooney–Rivlin hyperelastic constitutive model was employed to characterize the encapsulation material, with $C_{Ecoflex10}$ = 8 kPa, $C_{Ecoflex01}$ = 2 kPa and $D_{Ecoflex}$ = 0.002 kPa^{-1} (corresponding to initial Young's modulus $E_{Ecoflex}$ = 60 kPa and Poisson's ratio $\nu_{Ecoflex}$ = 0.49)[66]. For stretching, twisting and bending simulation, the circuit board was fixed, and the displacements and rotations were applied to the panel. For the contact simulation of the panel to the skull, a uniform pressure was applied to the panel until all μ-ILEDs contacted the skull. The element number in the model was approximately 6×10^5, and the minimal element size was about one-fourth of the width of the narrowest copper trace (12 μm). Geometric nonlinearities were considered in the simulation. The finite element mesh convergence of the simulation was validated for all cases.

Electromagnetic modeling and power characterization

To confirm that the magnetic field within the cages was substantial and uniform for the behavior experiments, the software COMSOL (COMSOL 6.0) was used for the characterization of the double-loop antenna configuration. An adaptive mesh composed of tetrahedron elements and a spherical surface with a radius of 1,000 mm was employed as the radiation boundary to ensure computational precision. For the numerical modeling, the relative dielectric constant of air was set to 1, and the conductivity of copper was set to 5.8×10^7 S m^{-1}. To evaluate the normalized magnetic induction intensity on different planes of the cage, the current flowing through the copper wires was set to 1 A.

Optical characterization

The optoelectronic characterization of μ-ILED began by obtaining the corresponding current–voltage (I–V) characteristics using a

semiconductor device analyzer (Keysight, S1500A) interfaced with a probe station (Signatone, 1160). Then, measurements of μ-ILED current during wireless operation, combined with obtained I–V characteristics, yielded the electrical power of μ-ILED with respect to the power supplied to the transmission antenna. An integrating sphere photodiode power meter (Thorlabs, S140C) in combination with a calibrated power meter (Thorlabs, PM100D) served to characterize the optical power generated by the μ-ILED. A current source (Tektronix, Inc., Keithley 6221) powered the μ-ILED after insertion into the integrating sphere, with applied current from 1 mA to 20 mA with a 1-mA interval. This result, combined with μ-ILED I–V characteristics and current during operation, yielded the μ-ILED efficiency and output intensity with respect to the transmission antenna power.

For measurements involving light attenuation in brain tissue, a patch cable (600-μm core, numerical aperture 0.37; Doric) attached to an optical fiber (600-μm core, numerical aperture 0.37, 6 mm long) relayed the signal to the integrating sphere for recording the intensity. The isolated mouse skull and brain tissues, affixed to the μ-ILED array, were positioned on a metal block on a stereotaxis that also secured the optical fiber. With 0.1-mm precision, the optical fiber advanced through the skull base and brain, and light intensity readings were recorded at each depth until the fiber tip reached the pia. The absolute intensity readout was normalized to the maximum intensity at the pia level, providing the light attenuation ratio in the brain tissue at each depth. Subsequent measurements of post-skull optical penetration efficiency followed the same procedures, incorporating an additional piece of mouse skull affixed to the μ-ILED exposure surface when using the integrating sphere for measurements of optical power for the μ-ILED with varying inputs.

Thermistor fabrication and thermal characterization

To measure the temperature load in the surrounding structures of the optical–neural interface, a thin-film thermistor was fabricated using standard photolithography[67]. Fabrication of the thin-film thermistor began by spin-coating polymethyl methacrylate (PMMA; 500 nm) and polyimide (5 μm) on a silicon wafer substrate sequentially. Electron beam physical vapor deposition (EBPVD) then formed a thin conductive film of 20-nm Ti and 100-nm Au on the polyimide layer. Another spin-coating process formed a thin layer of photoresist (Microposit, S1813; approximately 1.5 μm) on the metal layers. A maskless aligner (Heidelberg Instruments, MLA 150) patterned the photoresist layer into the desired geometry that contains sensors and connection traces. Sequential wet etching using Au etchant (Transene, Type TFA) and buffered oxide etch (Avantor, BOE 6:1) transferred the photoresist pattern to the underneath metal layers. After removing the remaining photoresist with acetone, a second layer of polyimide (5 μm) and a thin layer of Cu (60 nm) were deposited sequentially using spin-coating and EBPVD, respectively. A similar lithography and wet etching process (using Cu etchant) formed an etching mask on the Cu layer that encapsulated the patterns on the Ti/Au layers. A dry etching process using reactive ion etching (March RIE) transferred the Cu layer pattern to the underneath polyimide. Finally, the Cu mask was removed by Cu etchant.

Two clamps firmly held another same-size silicon wafer against the device silicon wafer with a tissue sandwiched in between. The wafers were then placed in an acetone bath in a glass beaker. A hotplate operated at 80 °C warmed the bath to accelerate the dissolution of PMMA. After 2 hours, a water-soluble tape transferred the device from the silicon wafer after careful removal of the top wafer and tissue. The thermistor was wired to a digital multimeter (National Instruments, USB-4065) after the removal of the backside water-soluble tape with deionized water. The temperature responses of the sensors underwent calibration using a data logger thermometer (OMEGA, HH374). The thin-film thermistor was then attached to the surface of the μ-ILED, skull and brain with epoxy glue to acquire temperature changes during μ-ILED operation.

Geometric modeling of cranial structures

The geometric models of the cranial structures were generated from an open-source database of rodent anatomical structures, corrected for C57/BL6 mice based on species-specific dimensional profiles. Original files (.stl) were converted to .stp and modeled using Abaqus. The FOD was reconstructed from the CAD file, mounting on the surface of modeled cranial structures. Additional materials, including cyanoacrylate adhesives, Norland 63, parylene-C, μ-ILEDs, fPCB and dental cement, are modeled in the full model. The geometric model was further converted into voxels and finite elements for optical and thermal simulation.

Optical simulations

The Monte Carlo method was used to simulate the optical profile for transcranial optogenetic stimulation[68,69]. Each volume in the numerical simulations consisted of $(400)^3$ voxels, with dimensions of $(12.5\ \mu m)^3$, filling a total volume of $(5\ mm)^3$. The red (628-nm) illumination source corresponding to the dimensions of the μ-ILED was set to $0.3 \times 0.3 \times 0.09\ mm^3$, featuring a Lambertian emission angle distribution:

$$L(\theta) = L_0 \cos\theta$$

$L(\theta)$ is the optical intensity. θ is the angle between the irradiation direction and the normal of the μ-ILED lower surface, which is 0.8 mm above the center of the numerical simulation volume. L_0 is the optical intensity for $\theta = 0$. The simulation launched 10^9 photons. The materials' optical properties, including absorption coefficients (μ_a), reduced scattering coefficients (μ_s) and refractive index (n), are summarized in Supplementary Table 2 for 628 nm. After performing the simulation for each volume of μ-ILED, postprocessing of the optical fluence rate yielded illumination profiles in three-dimensional space. The three-dimensional reconstruction of the transcranial illumination profiles resulting from 6.12-mW input optical power was generated using ParaView 5.7.0 (Kitware). The volume of μ-ILED co-illumination and crosstalk was then calculated based on input optical power and irradiance threshold for opsin excitation. The numerical model can be adapted for other wavelengths for which the optical properties of the brain have been characterized.

Thermal finite element analysis model

The transient-state thermal propagation considering the thermal load of the μ-ILEDs and the body heat flux caused by the optical power is defined by the governing equation[8,70,71]:

$$\begin{cases} \rho C_p \frac{\partial T}{\partial t} + \nabla \cdot (-k\nabla T) = Q_{\text{the}} + \phi\mu_a & \text{in}\Omega \\ q = h(T - T_\infty) & \text{on}\partial\Omega \end{cases}$$

Here, T is the temperature; ρ is the mass density; C_p is the heat capacity; and k is the thermal conductivity. Q_{the} is the heat source generated by the thermal load of the μ-ILEDs. ϕ is the optical fluence rate calculated in the optical simulation. Ω is the model region. The convective heat transfer boundary conditions are assigned on the boundary of this model region ($\partial\Omega$). q is the surface heat flux; T_∞ is the environmental temperature; and h is the convective heat transfer coefficient. Here, $h = 0.025\ mW\ mm^{-2}\ K^{-1}$ for the dental cement boundary, and $h = 0.005\ mW\ mm^{-2}\ K^{-1}$ for the skull boundary. Abaqus was used to compute the governing equation using the finite element method. Linear tetrahedral element was used, and the minimum edge length was 60 μm. The thermal conductivity (k), heat capacity (C_p) and mass density (ρ) of the materials are summarized in Supplementary Table 3. Additional measurements using a previously reported thermal actuator and multisensory (TAS) module[72] confirmed the thermal conductivity of essential biological and device materials.

Scanning electron microscopy

An FEI Quanta 650 environmental scanning electron microscope examined the surface morphology of the μ-ILED array and serpentine interconnects in high-vacuum secondary electron mode. An electron beam of 10 kV and a spot size of 3.0 were used. The surfaces of the samples were directly exposed to the electron beam during characterization.

Animals

Animals were handled according to protocols approved by the Northwestern University Animal Care and Use Committee. Wild-type C57BL/6 mice were obtained from Charles River Laboratories and bred in-house. Adult male and female mice, aged between postnatal days 80 and 120 and weighing 20–30 g at the onset of experiments, were used in the study. Prior to procedures, all mice were group housed, kept at approximately 25 °C with 30–70% relative humidity and maintained on a standard diet under a 12-hour light and 12-hour dark cycle (lights on at 6:00 or 7:00). A plastic igloo shelter and nesting materials were used as environmental enrichment. Littermates were randomly assigned to conditions. Mice were not involved in any previous procedures, and only healthy and immunocompetent mice were used.

Stereotactic injections and device implantation

Mice were anesthetized with isoflurane (3% for induction, 1.5–2% for maintenance) and fixed on a small animal stereotaxic frame (David Kopf Instruments) for intracranial injections. Analgesia included bupivacaine, meloxicam and buprenorphine-ER. AAV1.Syn–ChrimsonR–tdTomato (1×10^{13} GC ml^{-1}; Addgene viral prep no. 59171-AAV1, a gift from Edward Boyden) or AAV8.FLEX.tdT (1×10^{13} GC ml^{-1}; Addgene viral prep no. 28306-AAV8, a gift from Edward Boyden) mixed with AAV1.hSyn.Cre.WPRE.hGH (1×10^{12} GC ml^{-1}; UPenn Viral Core, a gift from James M. Wilson) was delivered through a pulled glass pipette (tip diameter 7–10 μm) for a total volume of 200 nl at a rate of 100–150 nl min^{-1} using an UltraMicroPump (World Precision Instruments). Injection coordinates for the motor cortex, primary somatosensory cortex (limbs), primary somatosensory cortex (trunk) and primary visual cortex are as follows: AP: +1.5, 0.0, −1.5 and −3.0 mm; ML: ± 2.0 mm; DV: −0.5 mm. Viral vectors were expressed for 2–4 weeks before device implantation.

Device implantation followed the procedure for back subdermal implantation reported previously[10]. Initially, an incision was made along the midline of the scalp to expose the skull. The FOD was positioned on the skull, aligning individual LEDs with the pre-made burred holes for viral injections. Subsequently, another 1-cm incision was made at the midline of the back, approximately at the T10-L1 level. The subcutaneous fascia between the scalp and back incisions was separated, and the wireless device was gently pulled from the scalp incision toward the lumbar spine. Serpentine interconnects linking the FOD and the electronic board were routed subcutaneously through the neck. After this, the incisions were sutured closed, and the animals were closely monitored and allowed to recover for several hours before being returned to the colony for appropriate post-surgical observation.

Tissue processing and histology

Mice were deeply anesthetized using isoflurane and subsequently underwent transcardial perfusion with 4% paraformaldehyde (PFA) dissolved in 0.1 M PBS. After perfusion, brains were post-fixed in 4% PFA at 4 °C and then rinsed in PBS before being sectioned at a thickness of 60 μm using a vibratome (Leica Biosystems). These sections were then mounted onto Superfrost Plus slides (Thermo Fisher Scientific), allowed to air dry and coverslipped using a mixture of glycerol and TBS in a 9:1 ratio, with Hoechst 33342 at a concentration of 2.5 μg ml^{-1} (Thermo Fisher Scientific). Sections were scanned using an Olympus VS120 slide scanning microscope (Olympus Scientific Solutions Americas) to assess the areas of viral expression.

Quantitative FISH

Quantitative FISH was performed following established protocols[73–75]. Hybridization chain reaction (HCR) RNA-FISH was conducted over 3 days. Mice were deeply anesthetized with isoflurane before decapitation. Brains were rapidly extracted, embedded in tissue-freezing medium and chilled on a dry ice–ethanol mixture before storage at −80 °C. Coronal brain sections (30 μm thick) were prepared using an Epredia NX70 Cryostat (Epredia), mounted on Superfrost Plus slides and stored at −80 °C until processing. Frozen sections were fixed in 4% PFA for 20 minutes at 4 °C, followed by dehydration in graded ethanol solutions (50%, 70% and 100%, 5 minutes each). Sections were then washed in 1× PBS and dried, and tissue boundaries were outlined with a hydrophobic pen. To reduce endogenous fluorescence, proteinase K digestion (10 μg ml^{-1} for 10 minutes at 37 °C) was performed. For hybridization, 100 μl of chilled hybridization buffer was applied to each slice, and slides were incubated at 37 °C for 10–12 minutes in a humidified chamber. Probe solutions (0.8 μl of each probe in 100 μl of hybridization buffer at 37 °C) were prepared and applied to slices before coverslipping. Hybridization was conducted overnight at 37 °C in a humidified chamber. Coverslips were gently removed in HCR probe wash buffer, and sections underwent post-hybridization washes with decreasing ratios of probe wash buffer to SSCT (75%, 50%, 25% and 0%) for 15 minutes each at 37 °C. Chilled amplification buffer (200 μl per slice) was applied for pre-amplification at room temperature (35 minutes). For amplification, hairpin solutions (h1 and h2) were prepared by snap cooling (95 °C for 90 seconds), diluted in amplification buffer (2 μl of each hairpin in 100 μl of amplification buffer), applied to slices and coverslipped. Incubation occurred overnight at room temperature in a dark humidified chamber. Coverslips were gently removed in 5× SSCT, and unbound probes were washed twice in fresh 5× SSCT (30 minutes each). Slides were dried, mounted with ProLong Gold antifade reagent containing DAPI (Molecular Probes) and coverslipped. Mounted slides were dried overnight before imaging, which was performed within a few days.

Confocal images were acquired using an Olympus FV3000 confocal microscope or a Leica SP8 confocal microscope with ×60/×63 objectives (oil immersion). Three/four-channel *z*-stacks (512 × 512 pixels, 0.5-μm intervals between slices) were collected, covering the entire cortical column (layers 1–6) at sites with the highest ChrimsonR (tdTomato) expression. FISH images were analyzed using Fiji. Cortical layers were categorized based on distance from the cortical surface (L1: 1–100 μm, L2/3: 100–300 μm, L4: 300–400 μm, L5a: 400–500 μm, L5b: 500–700 μm, L6a: 700–900 μm). All channels were thresholded, and cellular ROIs were defined based on DAPI signals to identify cell nuclei. Within these ROIs, FISH puncta were quantified. Cells were classified as marker positive if they surpassed a transcript-specific puncta threshold (for example, >5 puncta per soma for *Vgat*$^+$ cells). Although these stringent criteria minimized false-positive co-localization, they may have underestimated populations expressing low-abundance transcripts due to limitations in detecting sparse signals. For quantitative analysis of *fos* and *tdTomato* transcripts, the integrated density of puncta within each ROI was quantified across all experimental conditions using Fiji (ImageJ)[76]. To establish thresholds for *fos*$^+$ and *tdTomato*$^+$ populations, *k*-means clustering was applied, allowing separation of the grouped population into *fos*$^{+/-}$ and *tdTomato*$^{+/-}$ subgroups.

In vivo electrophysiology recordings

Mice previously injected with AAV1–Syn–ChrimsonR–tdTomato were anesthetized with vaporized isoflurane (3% for induction, 1.5–2% for maintenance) and fixed on a small animal stereotaxic frame (David Kopf Instruments). A 1.0-mm craniotomy window was opened over either the previously injected limb or the trunk area of the somatosensory cortex: AP: 0.0 and −1.5 mm, ML: ±2 mm. A stainless steel screw (18-8 button head torx screw; McMaster-Carr, 90910A600) with an attached length of silver wire (0.375-mm diameter; Warner Instruments, 64-1320)

was screwed into the contralateral occiput as an electrical reference. A custom-made headplate was attached to the animal's skull and fixed to the stereotaxic frame to ensure stability during the recording.

A four-shank, 64-channel MEA (shanks spaced 250 µm apart, electrodes spaced 50 µm vertically; NeuroNexus Technologies, A4x16_5mm_250-177) was inserted into the cortex through the craniotomy so that the bottom electrode of each shank was 750 µm below the surface. The MEA was connected to an analog-to-digital amplifier (Intan Technologies, C3325) that was affixed to the stereotax. The array was oriented parallel with the midline of the mouse. The craniotomy around the probe was covered with a mixture of mineral oil and glass ionomer powder to mimic the optical properties of the cranium.

A single µ-ILED was placed at the surface of the cranium at varying distances laterally from the MEA. The µ-ILED was held and manipulated using an additional stereotaxic arm, opposite to the MEA. Distances between each shank of the array and the µ-ILED were calculated with the Pythagorean theorem. Power to the µ-ILED was provided by a precision current source (Tektronix, Inc., Keithley 6221). At each distance, the µ-ILED was stimulated with 2-ms pulses at 4 Hz for 60 seconds at different optical irradiance. Then, 30-kHz data were simultaneously recorded from the MEA and the current source using an Open Ephys data acquisition board with the associated software (Open Ephys, GUI version 0.5.5)[77].

All data processing and analysis were done offline in Python. For spike analysis, stimulation and common-mode artifacts were removed using a version of the ERAASR algorithm[29]. For each recording, we started with a T (timepoints across recording) × C (number of channels) matrix M of continuous data. We performed principal component analysis on the continuous data to create the component matrix W. We removed the first four components as stimulation noise. To avoid removing portions of signal with the noise, for each channel C we created a version of the component matrix W_C for the first four components such that

$$W_C \begin{cases} 0 & \text{if } C = c \\ W & \text{otherwise} \end{cases}$$

We then re-projected the first four principal components using W_C to create artifact signal A_C, regressed the A_C original signal for channel C (M_C) using the normal equation and then subtracted it from M_C.

$$A_C = {W_C}^T M$$

$$\hat{M}_C = M_C - {A_C}^{-1} A_C M_C$$

The cleaned signal $\hat{M}$ was then acausally filtered with a 300–6,000-Hz bandpass Butterworth filter and sorted using the Kilosort4 Python package[78]. The results were manually inspected, and spike templates that appeared to be noise were rejected. Direct activation was analyzed by comparing the pre-stimulus mean firing rate for each sorted unit with its activity 2 ms immediately after each stimulation.

To directly isolate the stimulation artifact, we recorded ChrimsonR$^-$ mice while stimulating at distances of 1–5 mm, in 1-mm increments (Extended Data Fig. 7a). Except for the AAV, the surgical and recording setup was as above. The stimulation artifact ended 0.5 ms after the stimulus ended and was completely removed by ERAASR (Extended Data Fig. 7b). To control stimulation artifacts in the LFP analyses (Extended Data Fig. 7c–f), we excluded 3 ms of data immediately after stimulation start from analysis, based on observations in ChrimsonR$^-$ mice.

Experimental setup for behavioral studies

A host computer running a customized MATLAB script serves as the integrator of our wireless device with the open-source mouse operant chamber (Sanworks, Bpod 1030, developed by Josh Sanders). The system integration is as follows. The Bpod system comes with a dedicated library that interfaces with MATLAB, providing access to the sensors and actuators contained in the hardware of the operant chamber. For our wireless device, we developed a MATLAB library that communicates with the NFC radiofrequency module contained within the power distribution and control box (Neurolux, Inc., PDC Box) using a serial interface (RS232-to-USB converter). Using this library and the NFC reader/writer, we gained real-time control of the operation parameters of the NFC optogenetic device, such as programmable µ-ILED stimulation patterns and intensity, frequency, pulse widths and radiofrequency power of the PDC Box. The PDC Box drives a dual-loop antenna that wraps around the Bpod mouse operant chamber. Impedance and loading matching between the radiofrequency power module and the homemade radiofrequency antenna were controlled by an antenna tuner (Neurolux, Inc.) to ensure efficient power transmission and signal communication. The customized MATLAB scripts and the multisystem integration of technologies allowed to control the state machine of the Bpod to implement real-time adjustment of stimulation parameters based on behavioral feedback.

Water restriction

Mice started water restriction 5 days before training to motivate reward-seeking behaviors. The procedure began with recording initial body weight. Mice received 45% of the free drinking water requirement (2.8 ml per 30 g, daily) per Jackson Laboratory standards. The daily water supplement was calculated as 0.45 × 2.8 × (original body weight)/30 g. Mice were weighed and monitored daily for health status. If body weight dropped below 85%, additional water was provided (0.85 × original weight − current body weight). Water was dispensed in a plastic Petri dish in each home cage. During behavioral experiments, the total daily water included both the reward from the Bpod operant chamber and the extra amount given after sessions. Mice received their full calculated water requirement in their home cage if they did not engage in any reward-seeking behaviors[79].

Operant conditioning

The operant conditioning paradigm involved two phases: habituation pretraining before device implantation and stimulation training after implantation. During pretraining, mice were acclimatized to the operant chamber and trained to follow the trial structure. Each trial started when the mouse poked the center port, and a 10% sucrose water reward was provided after a second poke at either the left or right port. A white light at the center port served as a 'go' cue. As mice became more engaged in the task, the required holding time at the center port gradually increased to 1.0 second to initiate a trial. Once animals completed 100 trials within 30 minutes, they proceeded to the training phase after device implantation. In the stimulation training sessions, poking the center port triggered a sequential red light stimulation pattern from the µ-ILED array, consisting of four stimulation locations (20 Hz, 2-ms pulse width, 0.3 seconds at each location), with no inter-stimulus interval. The reward port remained unresponsive to premature pokes until the stimulation sequence was complete. After the stimulation sequence, a 'go' cue was given at the center port, and the animals were allowed to locate rewards. Initially, each mouse was assigned a 'target stimulation' pattern that remained constant throughout training, always indicating a reward on the left side. Incorrect choices resulted in an air puff punishment (<10 psi, 0.2 seconds). Mice advanced to the next task level upon achieving an 80% success rate or completing 2,000 trials at the current level. After completing the level 1–3 tasks, animals underwent a subset of probing/discrimination tasks with distractor stimuli designed to test their ability to distinguish between stimulation patterns with spatial or temporal differences. Supplementary Table 4 summarizes the target and non-target/distractor stimuli used in each task, number of sessions and related figure panels, arranged in the order from early to late stages of training. No left/right port bias correction methods

were employed. In all pretraining and training sessions, an external red light source was used to mask non-specific optical inputs from the environment and the FOD.

Open field locomotion

Locomotor activity was evaluated by placing mice in an open field arena under infrared illumination. Their movements were recorded for 15 minutes at 25 frames per second using a Raspberry Pi camera. To analyze locomotion, the animal's position—determined by its body center—was tracked using ToxTrac[80], which was then used to quantify the velocity, acceleration and exploration rate during the session.

Microscale computed tomography imaging

An animal implanted with the wireless optogenetic stimulator was euthanized and imaged with a preclinical microscale computed tomography (microCT) imaging system (Mediso, nanoScan scanner). Data acquisition parameters include medium magnification, 33-µm focal spot, 1 × 1 binning and 720 projection views (300-ms exposure time) over a full circle. Reconstruction of the projection data used a voxel size of 68 µm and post-processed with Mediso Nucline (version 2.01).

Statistics and reproducibility

Required sample sizes were estimated based on previous publications and experience[73,74,81]. At least two independent internal replications are included in the study. The number of biological replicates, trials and animals is reported in the figure legends. Animals were randomly assigned to treatment groups, and no data were excluded from analyses. The investigators were not blinded to allocation during experiments and outcome assessment, as all metrics were quantified and analyzed using automated pipelines applied identically across experimental groups. Group statistical analyses were done using GraphPad Prism version 7 (GraphPad Software). All data are expressed as mean ± s.e.m., box-and-whisker plots (minimum, first quartile, median, third quartile and maximum) or individual plots. Statistical significance was determined by one-sample *t*-test for one-group comparison versus 0.5 and two-tailed Student's *t*-tests for two-group comparisons, and one-way or two-way ANOVA tests were used for normally distributed data, followed by post hoc analyses for multiple group comparisons, as noted in the legends. $P < 0.05$ was considered statistically significant.

Reporting summary

Further information on research design is available in the Nature Portfolio Reporting Summary linked to this article.

Data availability

Raw data generated during the present study are available from the corresponding authors upon reasonable request. The analyzed data are available at https://doi.org/10.5281/zenodo.14880024 (ref. 82). Data supporting the findings of this study are included within this paper and its Supplementary Information files. Source data are provided with this paper.

Code availability

All computer code and customized software generated during and/or used in the present study are available at https://doi.org/10.5281/zenodo.14880024 (ref. 82).

References

62. Lu, L., Leanza, S. & Zhao, R. R. Origami with rotational symmetry: a review on their mechanics and design. *Appl. Mech. Rev.* **75**, 050801 (2023).
63. He, D., Malu, D. & Hu, Y. A Comprehensive review of indentation of gels and soft biological materials. *Appl. Mech. Rev.* **76**, 050802 (2024).
64. Yan, P., Huang, H., Meloni, M., Li, B. & Cai, J. Mechanical properties inside origami-inspired structures: an overview. *Appl. Mech. Rev.* **77**, 011001 (2025).
65. Christensen, R. M. Review of the basic elastic mechanical properties and their realignment to establish ductile versus brittle failure behaviors. *Appl. Mech. Rev.* **75**, 030801 (2023).
66. Huang, Y. et al. Microfluidic serpentine antennas with designed mechanical tunability. *Lab Chip* **14**, 4205–4212 (2014).
67. Wu, M. et al. Analysis and management of thermal loads generated in vivo by miniaturized optoelectronic implantable devices. *Device* https://doi.org/10.1016/j.device.2025.100898 (2025).
68. Fang, Q. & Boas, D. A. Monte Carlo simulation of photon migration in 3D turbid media accelerated by graphics processing units. *Opt. Express* **17**, 20178 (2009).
69. Zhang, H. et al. Analytical solutions for light propagation of LED. *Proc. Natl Acad. Sci. USA* **122**, e2508163122 (2025).
70. Deshpande, V. S. & McMeeking, R. M. Models for the interplay of mechanics, electrochemistry, thermodynamics, and kinetics in lithium-ion batteries. *Appl. Mech. Rev.* **75**, 010801 (2023).
71. Zhao, W., Liu, L., Lan, X., Leng, J. & Liu, Y. Thermomechanical constitutive models of shape memory polymers and their composites. *Appl. Mech. Rev.* **75**, 020802 (2023).
72. Kwon, K. et al. Wireless, soft electronics for rapid, multisensor measurements of hydration levels in healthy and diseased skin. *Proc. Natl Acad. Sci. USA* **118**, e2020398118 (2021).
73. Wu, M. et al. Attenuated dopamine signaling after aversive learning is restored by ketamine to rescue escape actions. *eLife* **10**, e64041 (2021).
74. Wu, M., Minkowicz, S., Dumrongprechachan, V., Hamilton, P. & Kozorovitskiy, Y. Ketamine rapidly enhances glutamate-evoked dendritic spinogenesis in medial prefrontal cortex through dopaminergic mechanisms. *Biol. Psychiatry* **89**, 1096–1105 (2021).
75. Xiao, L., Priest, M. F., Nasenbeny, J., Lu, T. & Kozorovitskiy, Y. Biased oxytocinergic modulation of midbrain dopamine systems. *Neuron* **95**, 368–384 (2017).
76. Schindelin, J. et al. Fiji: an open-source platform for biological-image analysis. *Nat. Methods* **9**, 676–682 (2012).
77. Pachitariu, M., Sridhar, S., Pennington, J. & Stringer, C. Spike sorting with Kilosort4. *Nat. Methods* **21**, 914–921 (2024).
78. Siegle, J. H. et al. Open Ephys: an open-source, plugin-based platform for multichannel electrophysiology. *J. Neural Eng.* **14**, 045003 (2017).
79. Pinto, L. et al. An accumulation-of-evidence task using visual pulses for mice navigating in virtual reality. *Front. Behav. Neurosci.* **12**, 36 (2018).
80. Rodriguez, A. et al. ToxTrac: a fast and robust software for tracking organisms. *Methods Ecol. Evol.* **9**, 460–464 (2018).
81. Wu, M. et al. Dopamine pathways mediating affective state transitions after sleep loss. *Neuron* **112**, 141–154 (2024).
82. Wu, M. et al. Data and code for the article 'Patterned wireless transcranial optogenetics generates artificial perception'. *Zenodo* https://doi.org/10.5281/zenodo.14880024 (2025).

Acknowledgements

We thank L. Butler for mouse colony management and F. Valero-Cuevas for meaningful insights and discussions. This work made use of the NUFAB facility of Northwestern University's NUANCE Center, which has received support from the SHyNE Resource (National Science Foundation (NSF) ECCS-2025633), the International Institute for Nanotechnology and Northwestern's Materials Research Science and Engineering Center program (NSF DMR-2308691). MicroCT imaging work was performed at the Northwestern University Center for Advanced Molecular Imaging (RRID: SCR_021192), generously supported by National Cancer Institute Cancer Center

Support Grant P30 CA060553 awarded to the Robert H. Lurie Comprehensive Cancer Center. Microscopy analyses using Leica SP8 were performed at the Biological Imaging Facility at Northwestern University (RRID: SCR_017767), generously supported by the Chemistry for Life Processes Institute, the Northwestern University Office for Research, the Department of Molecular Biosciences and the Rice Foundation. This work was funded by the Querrey-Simpson Institute for Bioelectronics (M.W., Y.Y., A.I.E., A.V.-G., Y.W., J.G., L.Z., J.L., M.K., J.K., Y.H. and J.A.R.); National Institute of Neurological Disorders and Stroke (NINDS)/BRAIN Initiative 1U01NS131406 (Y.K. and J.A.R.); National Institute of Mental Health (NIMH) R01MH117111 (Y.K.); NINDS R01NS107539 (Y.K.); 2021 One Mind Nick LeDeit Rising Star Research Award (Y.K.); Kavli Exploration Award (Y.K.); Shaw Family Pioneer Award; Center for Reproductive Science, Feinberg School of Medicine (J.M.C.); NIMH R00MH120047 (L.P.); Simons Foundation grant 872599SPI (L.P.); Alfred P. Sloan Foundation grant SP-2022-19027 (L.P.); North Carolina State University Start-up Fund 201473-02139 (A.V.-G.); 2T32MH067564 (J.Z.); and the Christina Enroth-Cugell and David Cugell fellowship (M.W.). The funders had no role in study design, data collection and analysis, decision to publish or preparation of the manuscript.

Author contributions

Conceptualization: M.W., Y.Y., Y.K. and J.A.R. Methodology: M.W., Y.Y., A.I.E., J.Z., A.V.-G., X.L., Y.K. and J.A.R. Theoretical simulations: X.L., K.Z., M.W., W.Z., A.V.-G. and Y.H. Investigation: M.W., Y.Y., J.Z., A.I.E., A.V.-G., X.L., K.Z., Y.W., K.L.B., J.G., M.R., G.W., M.K., L.Z., J.L., L.H.Y., H.Z., S.N.F., M.L., J.K., J.L.C., X.Z., H.S., K.T., S.C., Y.Z., A.B., C.H.G., J.M.C., L.P., Y.H., Y.K. and J.A.R. Software: A.V.-G., L.H.Y., Y.W., K.L.B. and M.R. Formal analysis: M.W., J.Z., X.L., K.Z., K.L.B. and L.H.Y. Validation: M.W., J.Z., A.I.E. and K.L.B. Data curation: J.Z., L.Z., L.H.Y., K.L.B. and A.I.E. Visualization: J.Z., M.W., Y.Y., A.I.E., X.L., K.Z., Y.W., J.G., J.L. and M.R. Supervision: Y.Y., Y.H., Y.K. and J.A.R. Funding acquisition: Y.H., Y.K. and J.A.R. Writing—original draft: M.W., Y.Y., J.Z., A.I.E., A.V.-G., X.L., K.Z., Y.K. and J.A.R. Writing—review and editing: M.W., Y.Y., J.Z., A.I.E., A.V.-G., X.L., K.Z., K.L.B., J.L., J.M.C., L.P., Y.H., Y.K. and J.A.R. M.W., Y.Y., J.Z., A.I.E., K.Z. and X.L. contributed equally to this work.

Competing interests

J.A.R. and A.B. are co-founders in a company, Neurolux, Inc., that offers related technology products to the neuroscience community. C.H.G. is employed by Neurolux, Inc. The other authors declare no competing interests.

Additional information

Extended data is available for this paper at https://doi.org/10.1038/s41593-025-02127-6.

Supplementary information The online version contains supplementary material available at https://doi.org/10.1038/s41593-025-02127-6.

Correspondence and requests for materials should be addressed to Yiyuan Yang, Abraham Vázquez-Guardado, Yonggang Huang, Yevgenia Kozorovitskiy or John A. Rogers.

Peer review information *Nature Neuroscience* thanks Luis Carrillo-Reid and the other, anonymous, reviewer(s) for their contribution to the peer review of this work.

https://doi.org/10.1038/s41593-025-02127-6

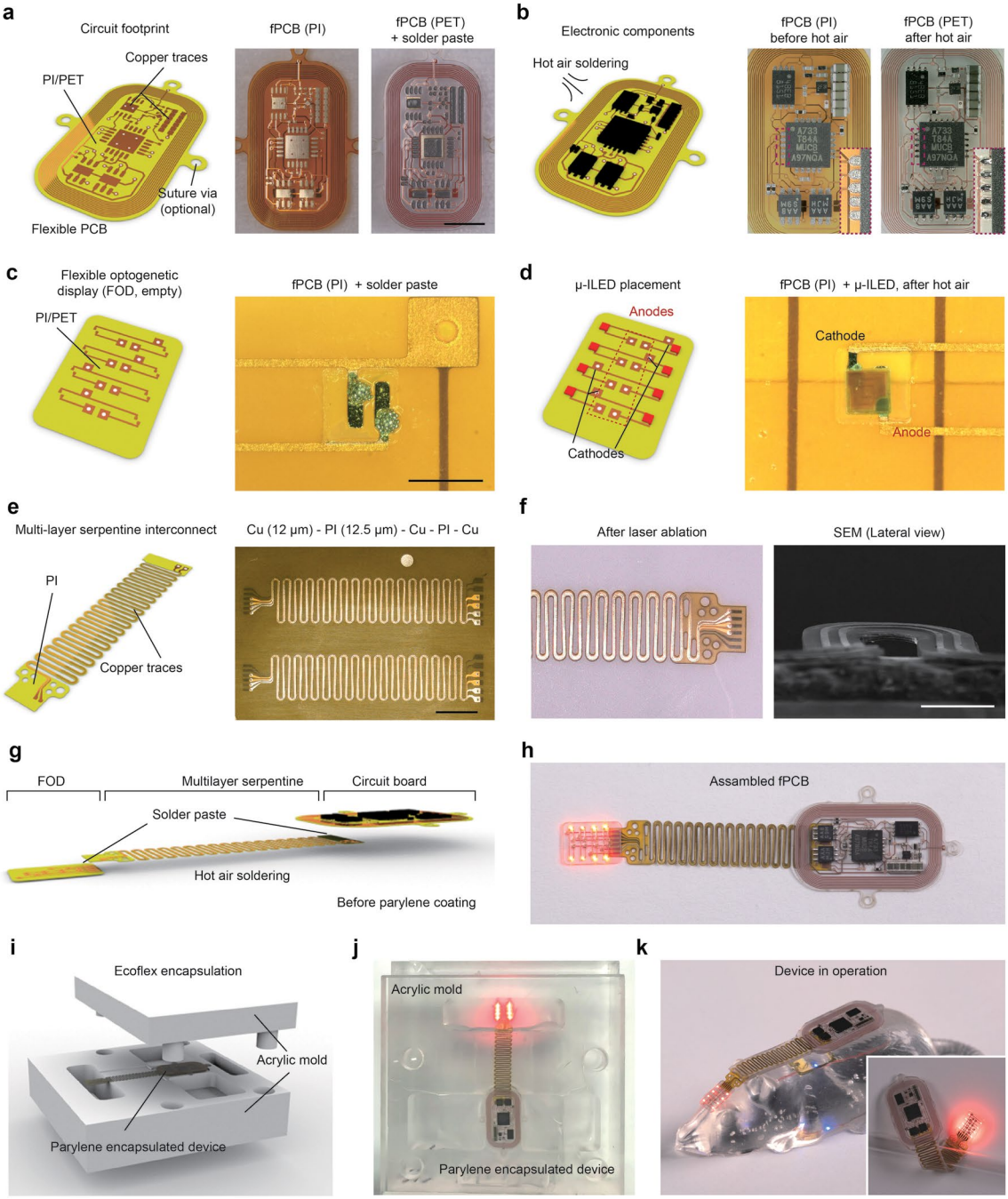

Extended Data Fig. 1 | Device fabrication and assembly. (**a**) Left, schematic illustration of the circuit base of the electronic module of the device using three-layer flexible printed circuit board (fPCB). Right, images of the fPCB for the electronic module. Scale bar: 5 mm. (**b**) Left, schematic illustration of the assembly of electronic components on the fPCB of the electronic module using hot-air soldering. Right, images of the electronic module after hot-air soldering of electronic components. (**c**) Left, schematic illustration of the circuit base of the FOD using three-layer fPCB. Right, magnified view of the soldering site for the μ-ILED with solder paste. Scale bar: 500 μm. (**d**) Left, schematic illustration of the FOD after hot-air soldering of the μ-ILEDs. Right, magnified view of the soldered μ-ILED. (**e**) Left, schematic illustration of the serpentine traces of the device using a five-layer fPCB. Right, image of the serpentine traces on the fPCB. Scale bar: 5 mm. (**f**) Left, image of the serpentine traces after laser ablation from the fPCB substrate. Right, scanning electron microscopic (SEM) image of the serpentine traces from lateral view. The experiment was repeated independently on 3 serpentine traces. Scale bar: 300 μm. (**g**) Schematic illustration of the final assembly of the electronic module, serpentine traces, and FOD. (**h**) Image of the final device after assembly. (**i**) Schematic illustration of the mold used for final silicone (Ecoflex 00-30) coating after parylene-C encapsulation. (**j**) Photograph of the device during mold casting of silicone. (**k**) Image of a fully encapsulated device ready for in vivo experiments.

https://doi.org/10.1038/s41593-025-02127-6

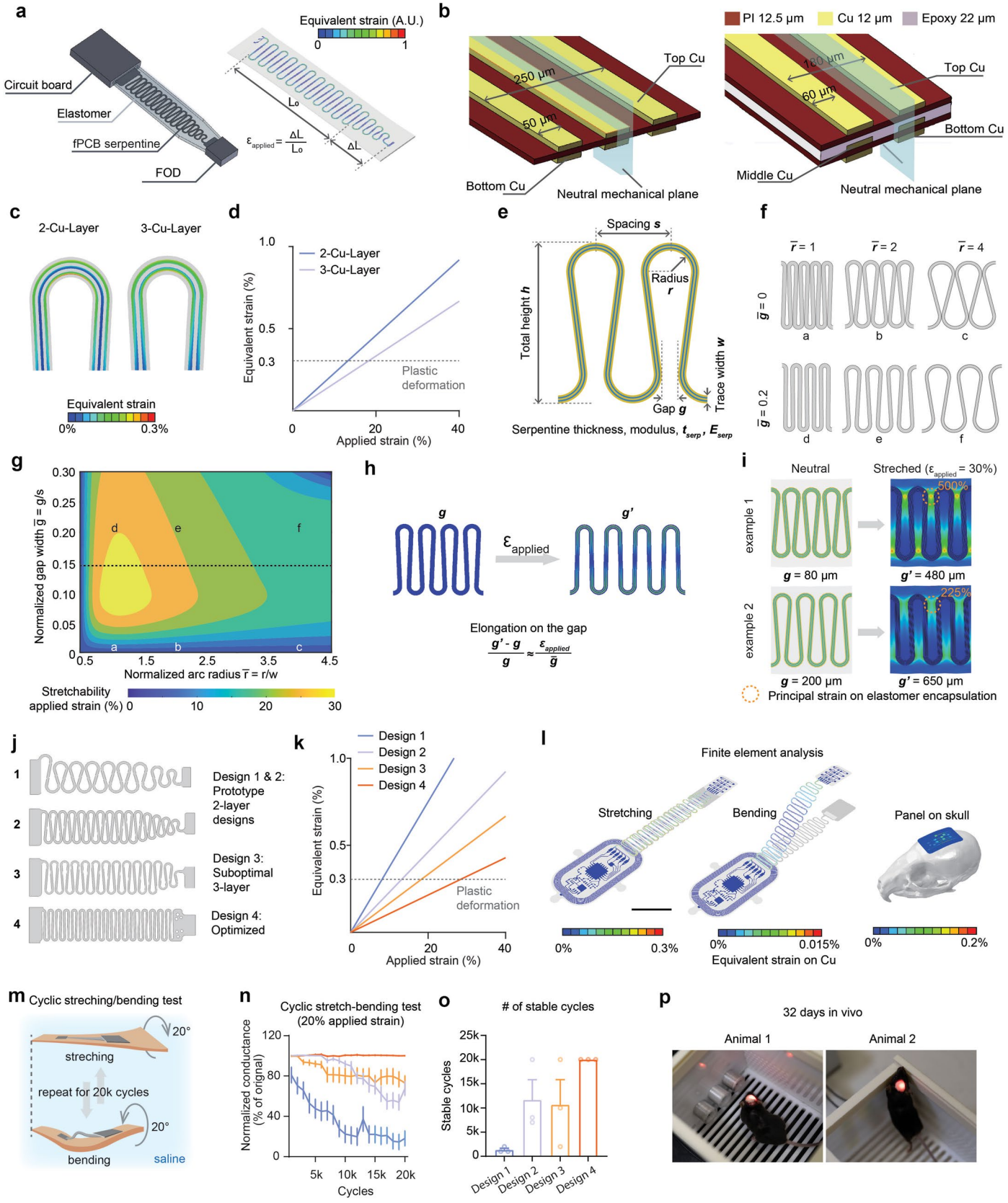

Extended Data Fig. 2 | See next page for caption.

https://doi.org/10.1038/s41593-025-02127-6

Extended Data Fig. 2 | Geometric optimization, numerical modeling, and experimental characterizations of serpentine interconnect. (**a**) Left, geometric model of structures surrounding the serpentine interconnect. Right, calculation of the applied strain on the serpentine and equivalent strain on the Cu-based serpentine conductive traces. (**b**) Layered structure of the serpentine materials relative to the neutral mechanical plane. Left: 2-Cu-layer design; right: 3-Cu-layer design. (**c**) Equivalent strain distribution on copper traces with 13% applied strain. (**d**) When a certain strain is applied to the serpentine interconnect, a certain copper unit on the trace shows the highest equivalent strain among all units. Summary graph showing this highest equivalent strain versus applied strains. Equivalent strain for copper plastic deformation equals 0.3%. (**e**) Geometric parameters that affect the stretchability of the serpentine interconnects. (**f**) Serpentine design examples with different gap widths and radius. (**g**) Contour map summarizing the stretchability as a function of normalized gap width and radius. Stretchability: maximal applied strain without causing plastic deformation on copper-based conductive traces. (**h**) Average elongation of the gap when the serpentine interconnect is stretched. (**i**) Elongation of the gap results in principal strain on the elastomer, causing potential encapsulation defects. (**j**) Design 1 & 2: prototypes, not guided by numerical modeling; Design 3, optimized layer structure with preliminary modifications of gap width and connecting regions; Design 4, optimized layer structure and geometry guided by numerical modeling. (**k**) Equivalent strain on the Cu-based conductive traces versus applied strain on the serpentine interconnect for the four designs. Dashed line: Equivalent strain threshold for plastic deformation on the copper traces. (**l**) Finite element analysis (FEA) of equivalent strain on the optimized serpentine interconnect under stretching (left) and bending (middle). Right, the equivalent strain on the FOD when flexed to the curvature of the skull. Scale bar: 10 mm. (**m**) Schematic illustration of the benchtop validation of the modeling outcomes using cyclic stretching and bending tests of devices integrated on artificial skin immersed in saline. (**n**) Summary data showing normalized conductance loads on individual μ-ILEDs for 20k cycles in cyclic stretching and bending tests. n = 21 pairs of traces from 3 devices for design 1; n = 27 pairs of traces from 3 devices for design 2; n = 26 pairs of traces from 3 devices for design 3; n = 20 pairs of traces from 3 devices for design 4. Data are presented as mean ± s.e.m. (**o**) Summary data for stable cycles where the devices maintain constant resistance during stretching and bending. n = 3 devices. Dots represent individual devices. (**p**) Images showing devices in operation in the Bpod chamber, 32 days after implantation.

https://doi.org/10.1038/s41593-025-02127-6

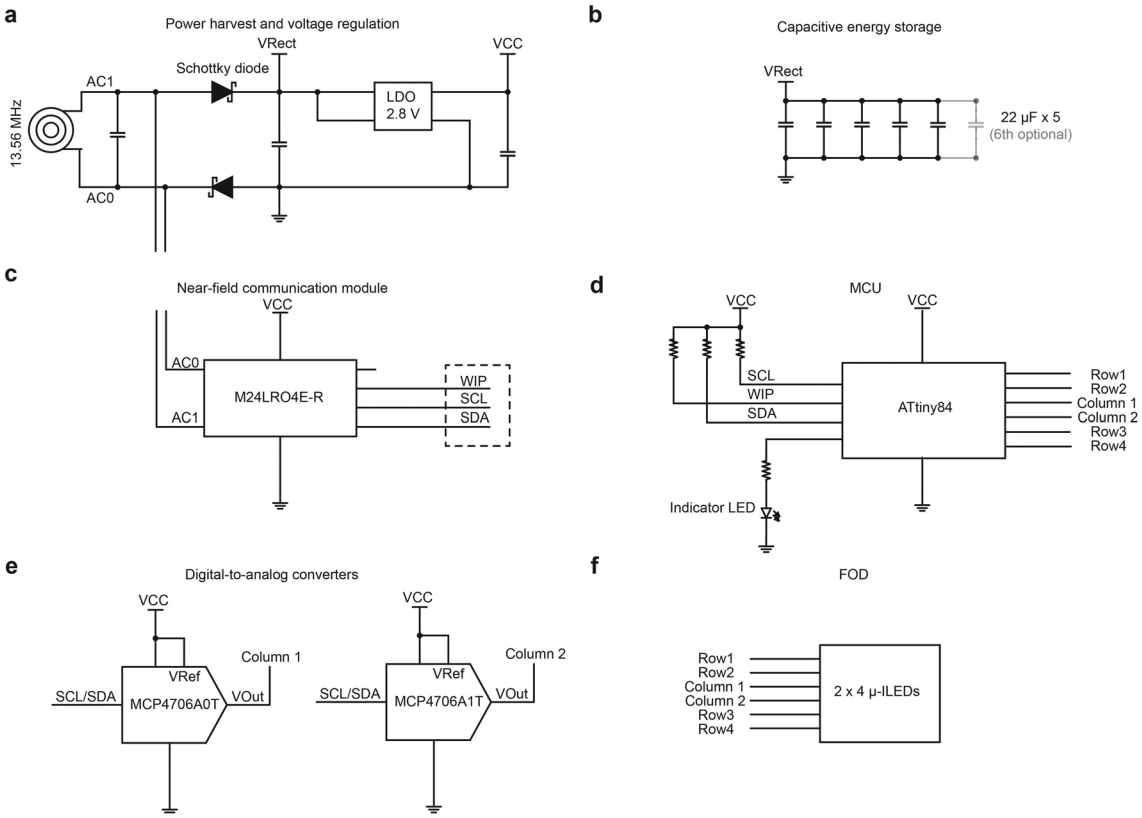

Extended Data Fig. 3 | Electronic modules for FOD with 2 × 4 configuration. (**a**) Schematic illustrations showing electronic circuits for wireless power harvesting and voltage regulation. (**b**) Capacitor bank for energy storage and discharge. (**c**) Near-field communication module for real-time programming. (**d**) Micro-controller circuit for parameter (order, frequency, duty cycle) control. (**e**) Digital-to-analog converters for intensity modulation. (**f**) FOD. Essential components and input/output pins are labeled on the schematics.

https://doi.org/10.1038/s41593-025-02127-6

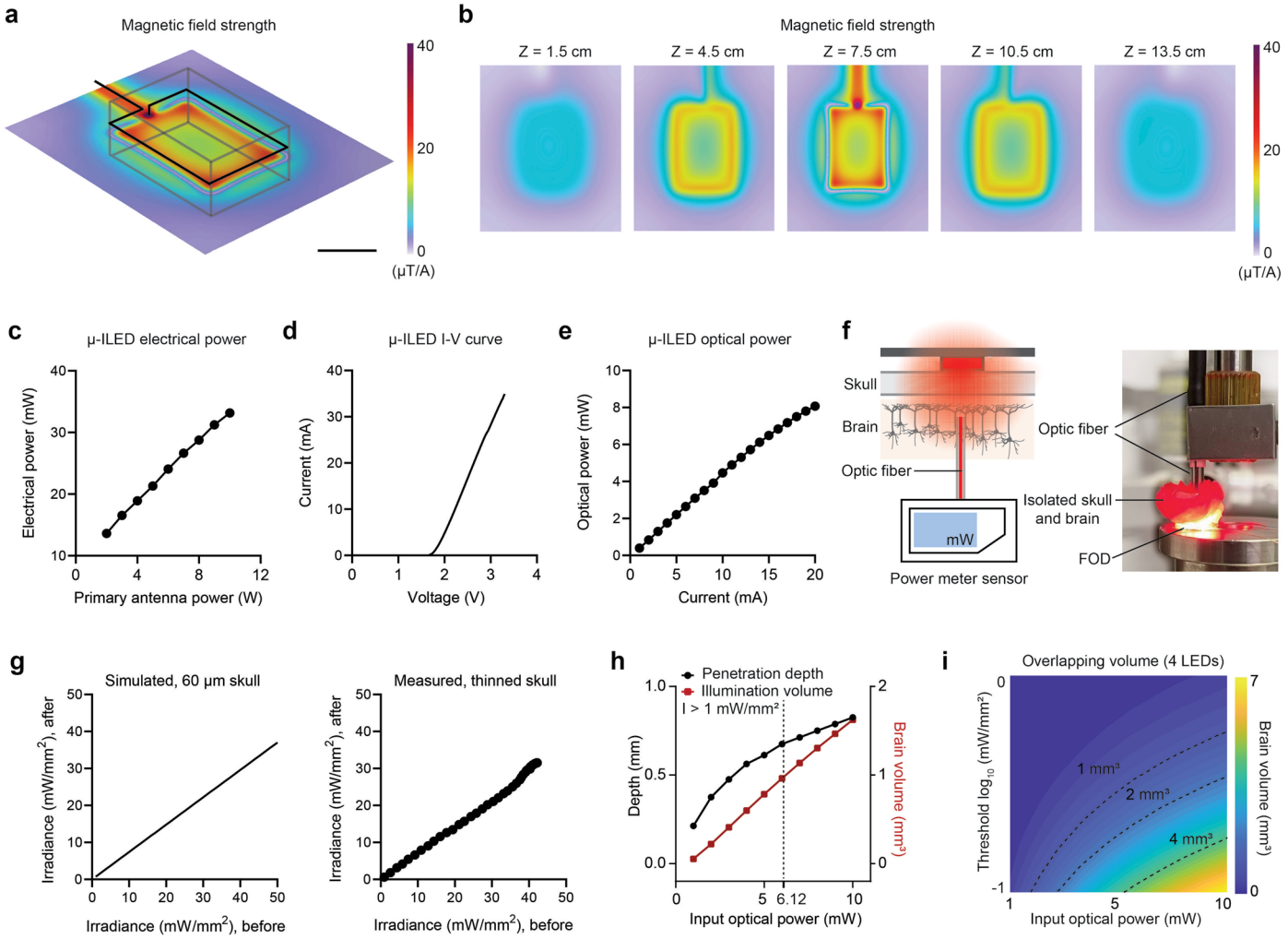

Extended Data Fig. 4 | Characterizations and validations for irradiance distribution profiles. (**a**) Simulated magnetic-field-intensity distribution at the central plane of a behavioral cage (dimensions, 20 cm (length) × 14 cm (width)) with a double-loop antenna at heights of 3 cm and 6 cm. Scale bar: 10 cm. (**b**) Simulated magnetic-field-intensity distribution at different heights in the Bpod behavioral cage. (**c**) The total electrical power of the μ-ILED with respect to the primary antenna power. (**d**) The I-V characterization for the μ-ILED. (**e**) The optical power of the μ-ILED with respect to the input current. (**f**) Schematic illustration (left) and image (right) of the experimental setup for measuring light attenuation through the skull and brain tissue. (**g**) Simulated (left) and measured (right) results of light attenuation through the skull. A 60 μm layer of skull was used in the numerical model. A piece of thinned skull was used for measurement. (**h**) Illumination volume and penetration depth as a function of the input irradiance of the red μ-ILED (628 nm). Threshold intensity, 1 mW/mm^2. (**i**) Contour map plot showing total overlap volume from 4 μ-ILED co-activation for different input optical power and intensity thresholds for opsin variants.

https://doi.org/10.1038/s41593-025-02127-6

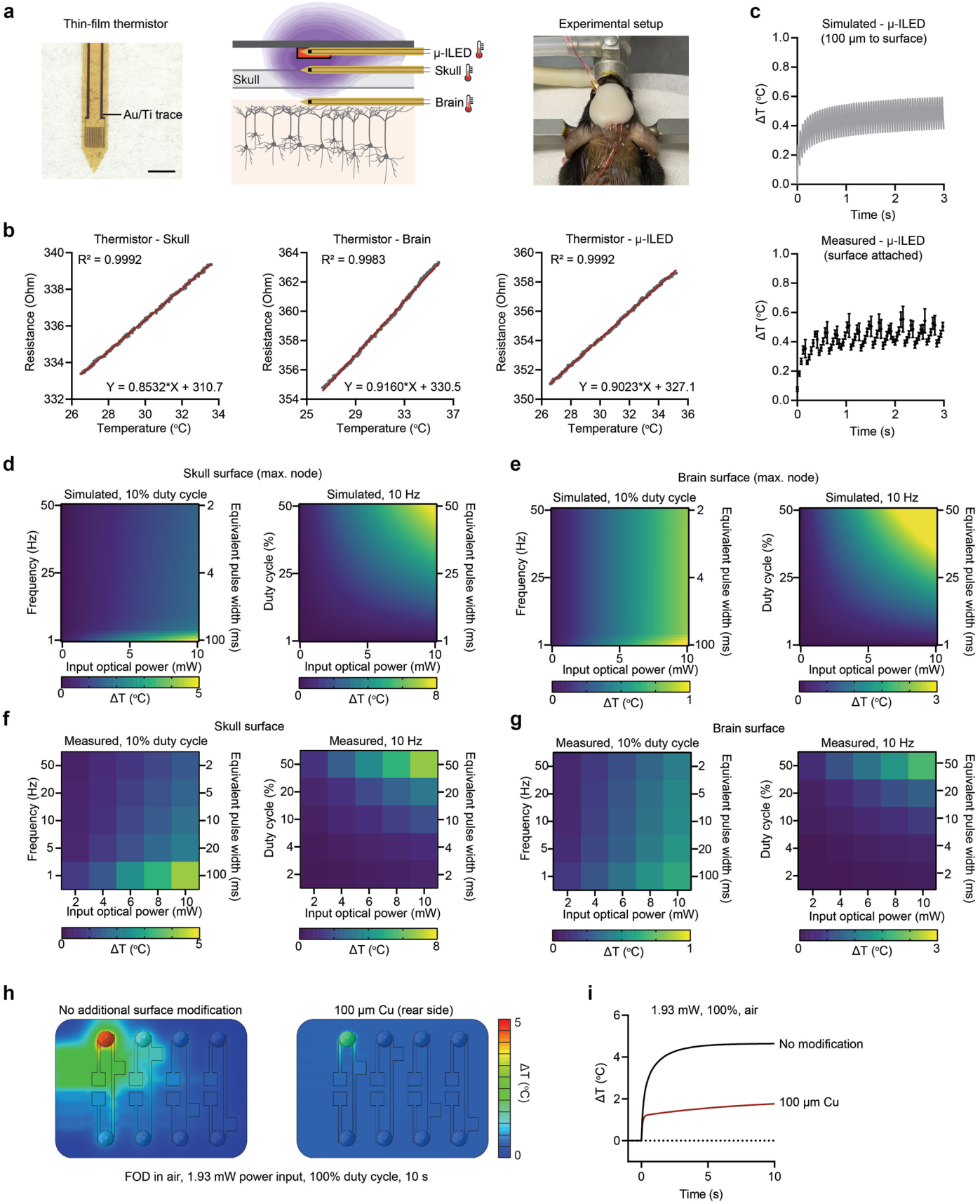

Extended Data Fig. 5 | See next page for caption.

https://doi.org/10.1038/s41593-025-02127-6

Extended Data Fig. 5 | Numerical and experimental assessments of heat accumulation to guide stimulation parameters. (**a**) Left, image of micro-fabricated thermistor for measuring temperature; middle, schematic illustration of the experimental setup for measuring heat accumulation in the structures surrounding the optical-neural interface; right, image of experimental setup, with wires connected to the thermistors to collect resistance value. Scale bar: 500 μm. (**b**) Calibration curves of thermistors used in this study for measuring the temperature increase on the surface of skull (left), on the surface of brain (middle), and below the μ-ILED (right). Each dot represents one resistance measurement at one temperature measurement. The best-fit line represents the linear regression between resistance and temperature. n = 1 representative thermistor at each location (skull, brain, or μ-ILED). (**c**) Simulated (Top) and measured (bottom) results of temperature increase below the μ-ILED for 3 s μ-ILED operation. The temperature increases in a $20 \times 300 \times 300\ \mu m^3$ volume, 100 μm below the μ-ILED surface, was output from the numerical model. The thermistor was manually placed and adhered to the μ-ILED surface, followed by a complete procedure of μ-ILED array fabrication. Measured data are presented as mean ± s.e.m. n = 3 technical replicates. Technical replicates are included to account for fluctuations in environmental temperature. (**d**) Left, simulated maximal temperature increases on the skull surface during μ-ILED operation with 10% duty cycle at varying frequencies. Right, same as left, but for varying duty cycles at 10 Hz. The finite element node with maximal temperature increase (max. node) was selected for plotting. (**e**) Same as (**d**), but for brain surface. (**f**) Left, measured temperature increases on the skull surface during μ-ILED operation with 10% duty cycle at varying frequencies. Right, same as left, but for varying duty cycles at 10 Hz. (**g**) Same as (**f**), but for brain surface. (**h**) Heatmap showing simulated heat production during a single μ-ILED operation in air at 100% duty cycle and 1.93 mW power for 10 s. Left, fPCB array patch without modification. Right, fPCB array patch coated with 100 μm Cu on the rear side. (**i**) Simulated temperature increases with or without device surface modification with 100 μm Cu.

https://doi.org/10.1038/s41593-025-02127-6

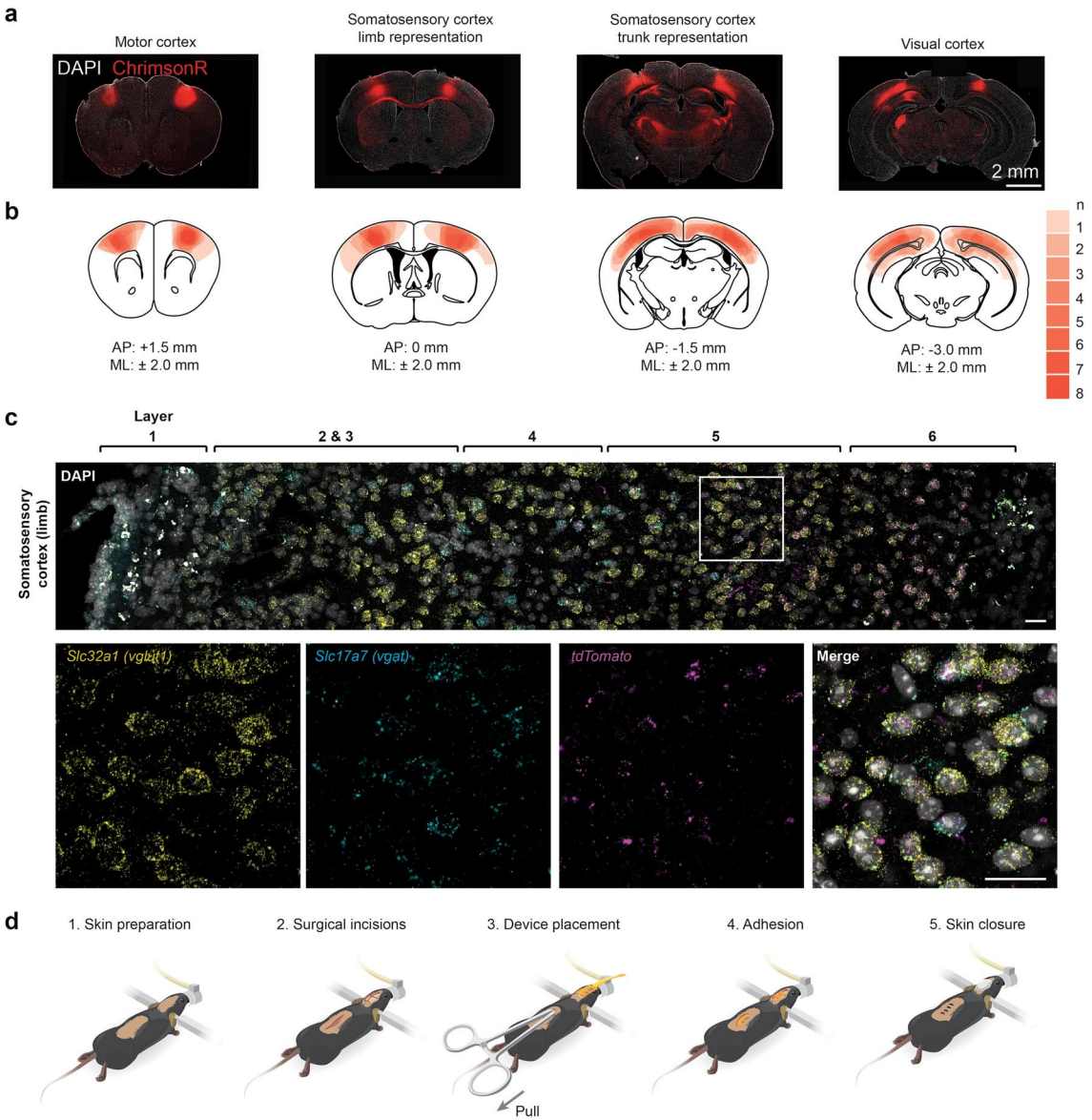

Extended Data Fig. 6 | Opsin expression and surgical procedures. (**a**) Representative images of ChrimsonR expression in the targeted cortical regions from one mouse. The experiment was repeated independently on 8 animals. (**b**) Heatmap showing the spread of viral expression across cortical regions. n = 8 animals. (**c**) Example image showing the distribution of *tdT*, *vglut1*, and *vgat* transcripts in cortical column of somatosensory cortex limb representation. L1, 1 to 100 µm, L2/3, 100 to 300 µm, L4, 300 to 400 µm, L5a, 400 to 500 µm, L5b, 500 to 700 µm, L6a, 700 to 900 µm. Scale bar, 25 µm. The experiment was repeated independently on 16 brain slices from 4 animals. (**d**) Schematic illustration of critical steps of surgical implantation.

https://doi.org/10.1038/s41593-025-02127-6

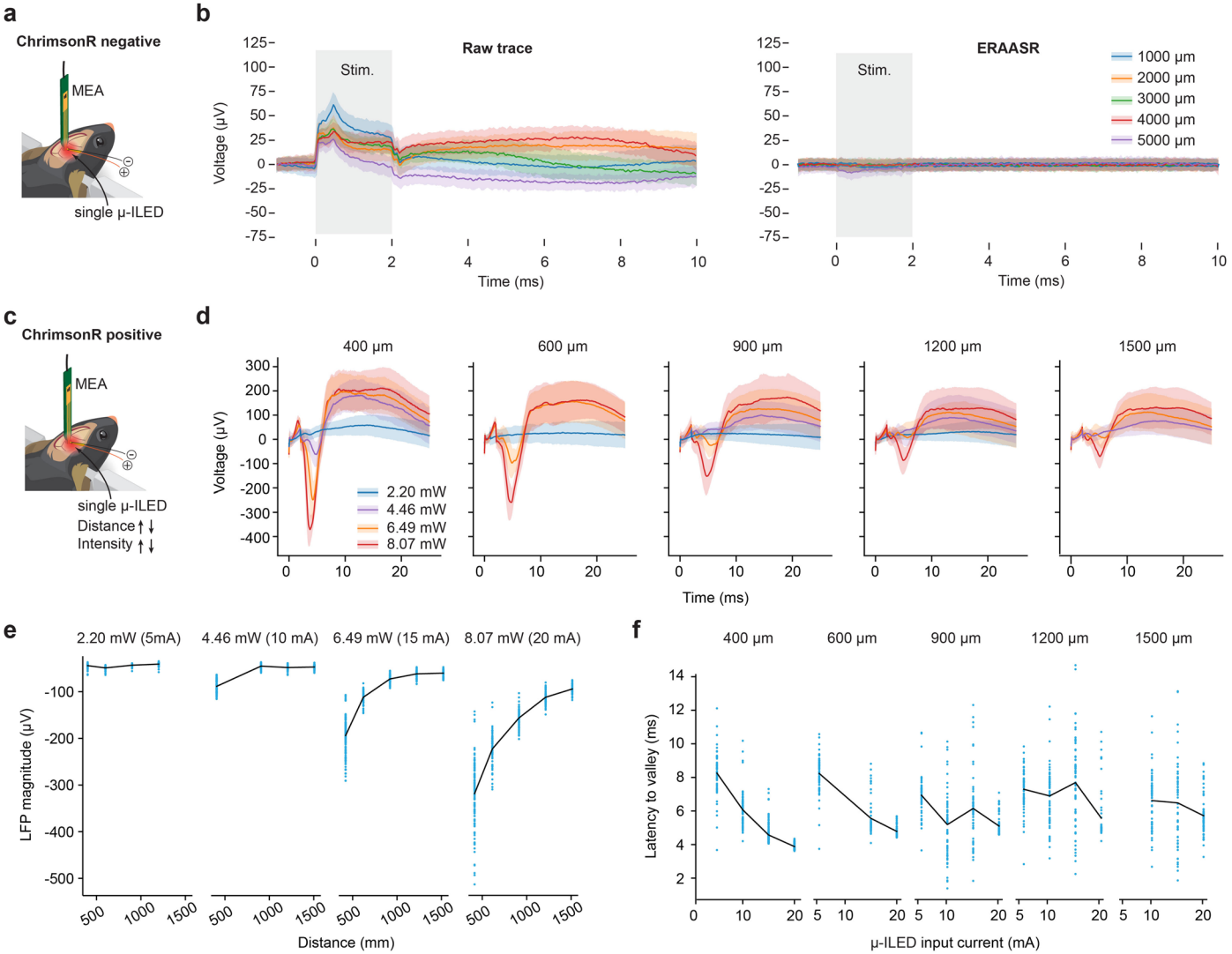

Extended Data Fig. 7 | Extracellular recording in ChrimsonR-negative mice and evoked local field potentials (LFPs) in ChrimsonR-positive mice. (**a**) Schematic of in vivo extracellular electrophysiology recordings in ChrimsonR-negative mice. (**b**) Left, raw recording traces showing the electrical artifacts during the stimulation period at different distances (1,000-5,000 µm) from µ-ILED. Right, processed traces using a custom-modified version of the Estimation and Removal of Array Artifacts via Sequential Principal Components Regression (ERAASR) algorithm. Lines and shaded areas represent mean ± s.e.m. (**c**) Schematic of the in vivo extracellular electrophysiology recording setup for evoked LFPs in ChrimsonR positive mice. (**d**) Traces showing evoked LFPs averaged across all electrodes of the MEA at different distances from the µ-ILED with varying input optical power. Lines and shaded areas represent mean ± s.e.m. (**e**) Summary of evoked LFP magnitudes at different distances from the µ-ILED under varying input optical power levels. Lines represent the mean from all electrodes, and dots indicate individual electrode measurements. (**f**) Same as (**e**), but for latency to valley in LFP waveforms. Dots represent individual electrodes; lines indicate the mean.

https://doi.org/10.1038/s41593-025-02127-6

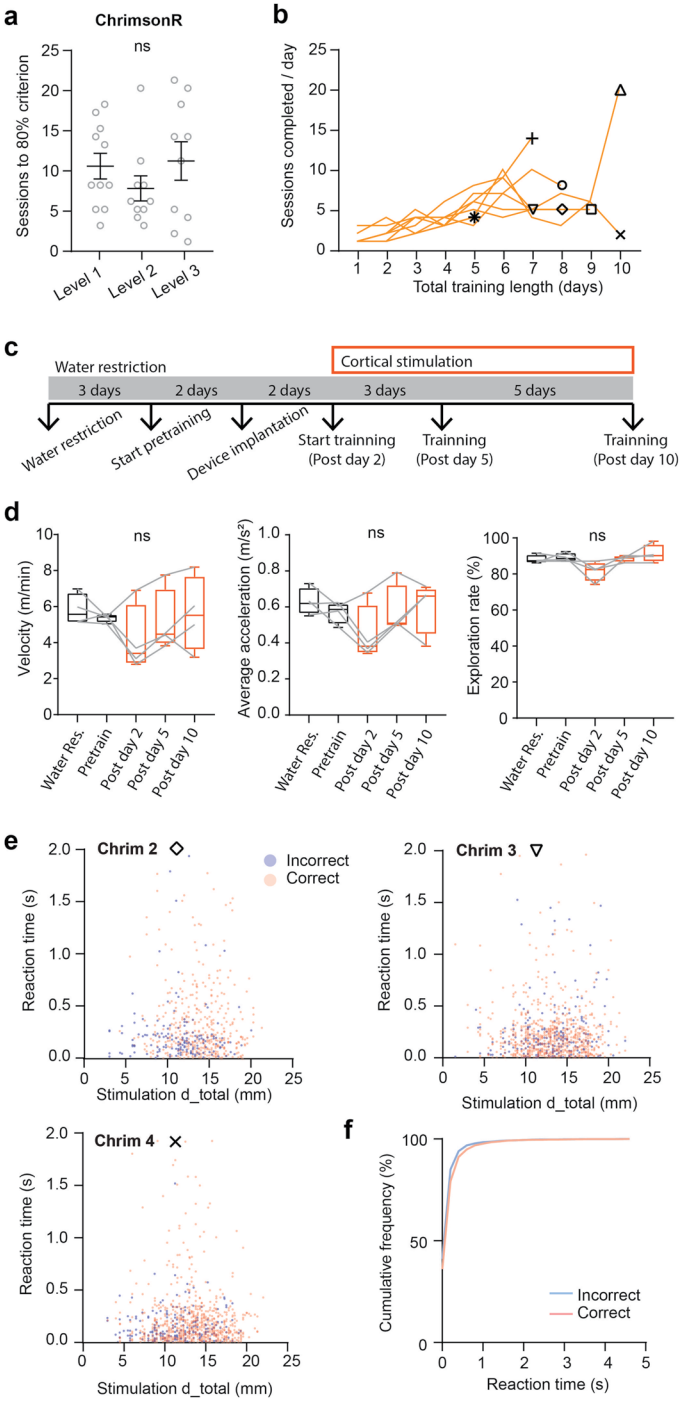

Extended Data Fig. 8 | Operant learning performance, reaction time analysis, and open-field locomotion analysis. (**a**) Number of sessions of 100 trials each across three levels of the task to reach the criterion of 80% success rate for animals expressing ChrimsonR (session median Level 1-12, Level 2-6, Level 3-12). One-way ANOVA, $p = 0.5750$, $F(2, 28) = 0.5645$; Sidak's multiple comparisons test, Level 1 vs Level 2, $p = 0.7258$; Level 2 vs Level 3, $p = 0.7596$; Level 1 vs Level 3, $p > 0.9999$; Level 1, n = 11 animals; Level 2, n = 10 animals; Level 3, n = 10 animals. Data are presented as mean ± s.e.m. Dots represent individual animals. (**b**) Summary data showing the total training length to complete Levels 1-3 and the number of sessions per day. Dark orange, group average; pale orange, individual trajectories; symbols mark the day individual animals reached criterion. (**c**) Timeline from water restriction to the end of training. Open-field locomotion was measured at the start of water restriction, before device implantation, and 2, 5, and 10 days post-implantation. (**d**) Left, average movement speed in an open-field arena across days, one-way ANOVA, $F(1.739, 5.217) = 1.632$, $p = 0.2773$. Middle, same as left, but for acceleration, one-way ANOVA, $F(2.154, 6.461) = 2.358$, $p = 0.1693$. Right, same as left, but for exploration rate, one-way ANOVA, $F(1.497, 4.491) = 3.271$, $p = 0.1354$. Box plots show median (line), 25th and 75th percentiles (bounds of box), minimum and maximum values (whiskers). n = 4 animals. (**e**) Scatter plots showing reaction times in all trials for the Level 3 task as a function of total cortical distance between stimulated digits. (**f**) Summary data of cumulative distributions of reaction times for all animals.

https://doi.org/10.1038/s41593-025-02127-6

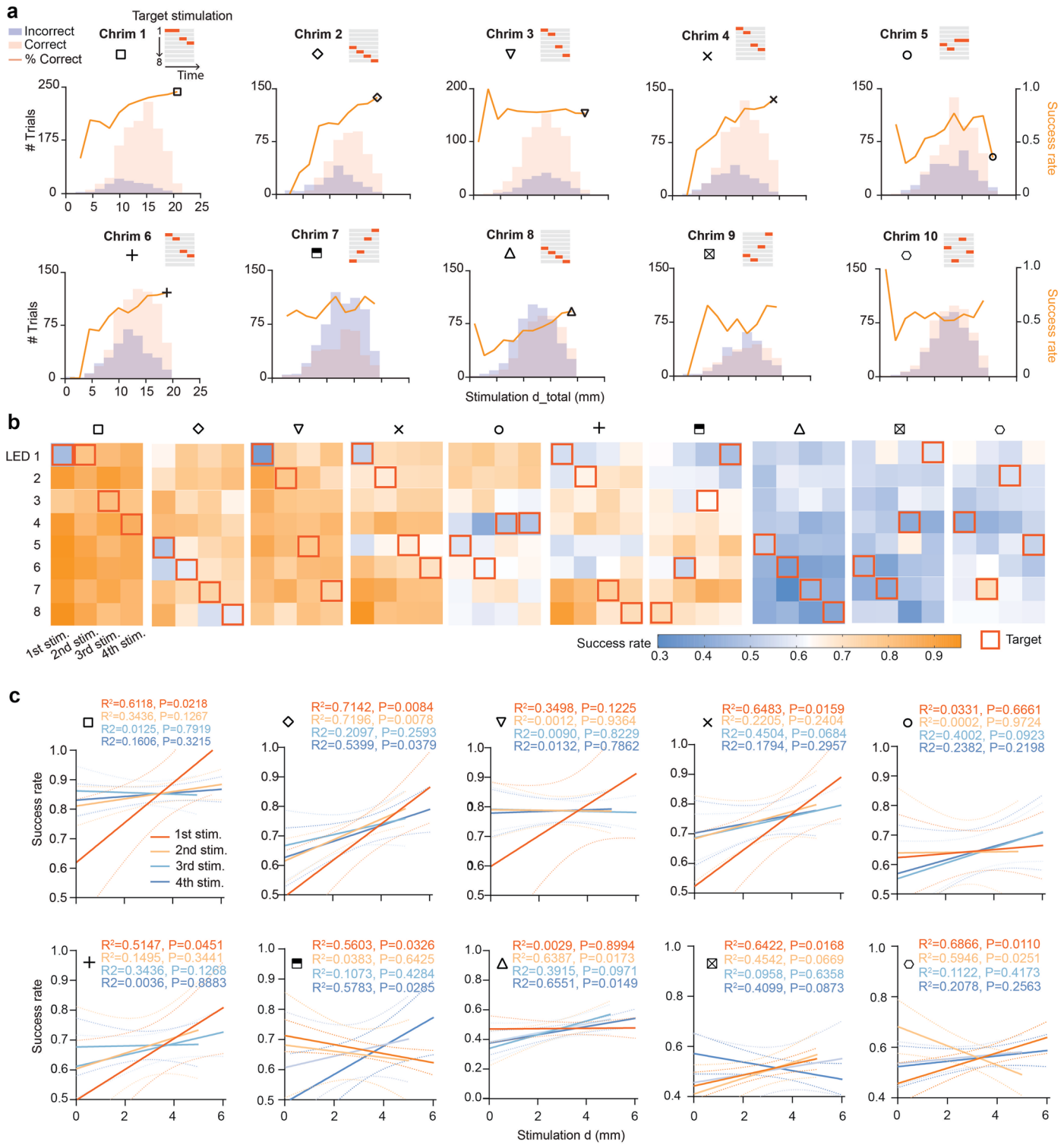

Extended Data Fig. 9 | Spatiotemporal analysis of behavioral trajectories for individual animals. (**a**) Line plots showing success rate as a function of spatial distance for 10 individual animals in the Level 3 task. The number of trials with correct or incorrect choices in each bin of spatial distance is plotted in the histogram. (**b**) Heatmap showing success rate for randomized non-target sequences grouped by specific stimulation locations at the first to the fourth stimulation digit in 10 ChrimsonR expressing animals. Red squares indicate the target stimulation sequence for each animal. (**c**) Two-sided Pearson's correlation analysis of spatial distance and success rate based on stimulation digit for individual animals. Dashed lines indicate 95% confidence intervals.

https://doi.org/10.1038/s41593-025-02127-6

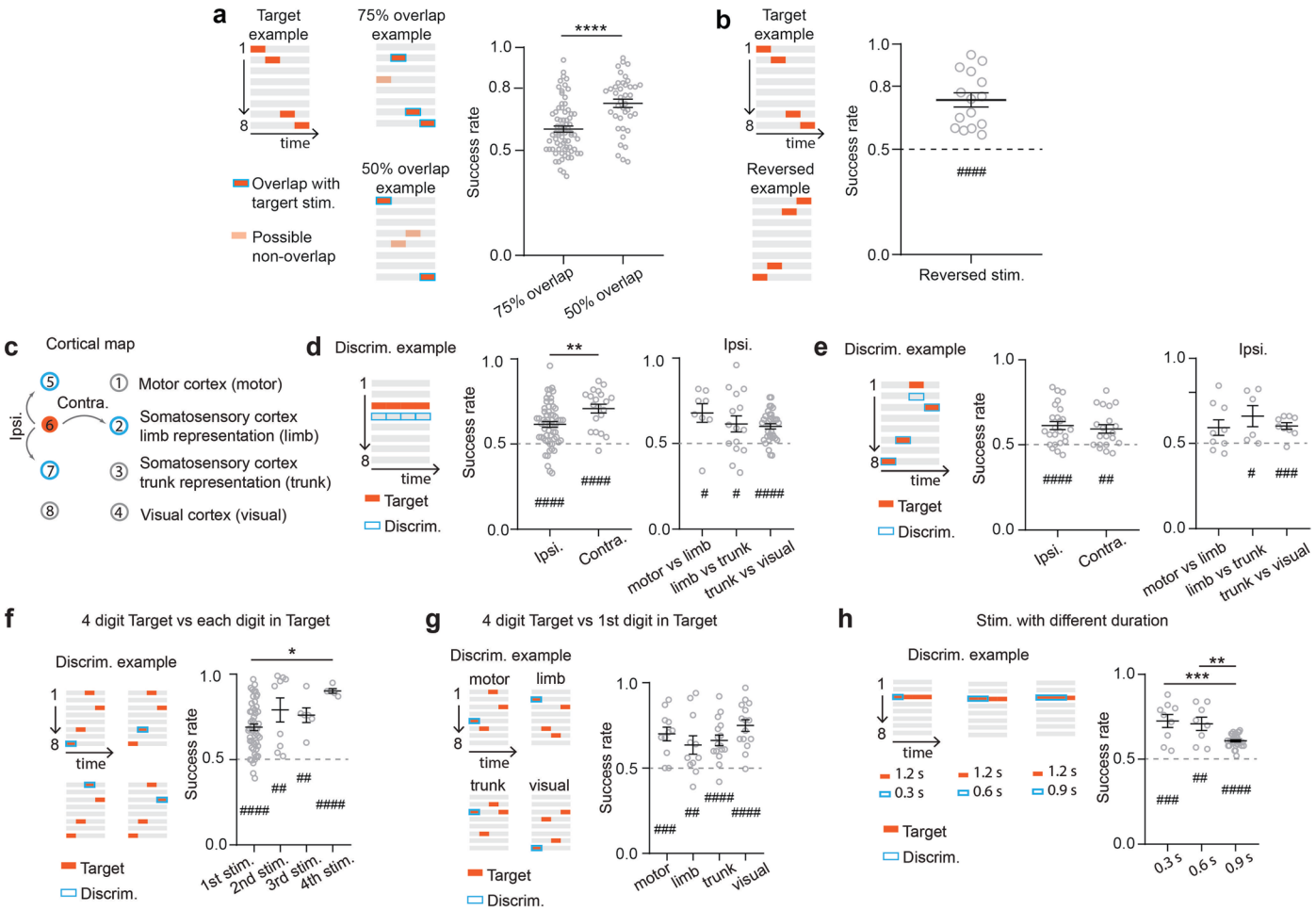

Extended Data Fig. 10 | Cue-discrimination of varying spatiotemporal patterns. (**a**) Left, schematic illustration of probing sequences with 75% (3 stimulation digits) and 50% similarity (2 stimulation digits) to the target sequences. Right, summary data showing the success rate of all probing sessions from all animals. 75% overlap, 0.6077 ± 0.0146; 50% overlap, 0.7312 ± 0.0203; Two-sided unpaired t-test, $p < 0.0001$. 75% overlap: n = 75 sessions from 5 animals; 50% overlap: n = 41 sessions from 5 animals. (**b**) Left, schematic illustration of probing experiments with reversed sequences. Right, summary data showing success rate of all probing sessions from all animals, 0.7347 ± 0.00338; One sample t-test vs 0.5, $p < 0.0001$; n = 15 sessions from 5 animals. (**c**) Schematic illustrating single site stimulation task for mice to discriminate neighboring stimulation either on the same hemisphere or on the contralateral hemisphere. (**d**) Left, example of target (stimulation on a single cortical region) and non-target stimulation on a neighboring site. Middle, summary data showing discrimination performance on neighboring stimulation sites. Ipsilateral, 0.6151 ± 0.0168; one sample t-test vs 0.5, $p < 0.0001$; n = 58 sessions from 5 animals. Contralateral, 0.7081 ± 0.0257; one sample t-test vs 0.5, $p < 0.0001$; n = 20 sessions from 3 animals; Two-sided unpaired t-test, ipsi vs contra, p = 0.0053. Right, summary data showing discrimination of ipsilateral neighboring stimulation, 1st column (motor vs limb), 0.6788 ± 0.0542; one sample t-test vs 0.5, p = 0.0132. 2nd column (limb vs trunk), 0.6147 ± 0.0471; one sample t-test vs 0.5, p = 0.0288. 3rd column (trunk vs visual), 0.6007 ± 0.0149; one sample t-test vs 0.5, $p < 0.0001$. One-way ANOVA, Sidak's multiple comparisons test, 1st vs 2nd column, p = 0.5884; 1st vs 3rd column, p = 0.3287; 2nd vs 3rd column, p = 0.9792. (**e**) Left, example of a target and a non-target stimulation, where one digit was switched to a neighboring site. Middle, summary data showing no significant difference in discrimination performance when the switched neighboring digit was in the ipsilateral or contralateral hemisphere. Ipsilateral, 0.6132 ± 0.0239; one sample t-test vs 0.5, $p < 0.0001$; n = 24 sessions from 3 animals. Contralateral, 0.5935 ± 0.0249; one sample t-test vs 0.5, p = 0.0013; n = 20 sessions from 3 animals; Two-sided unpaired t-test, ipsi vs contra, p = 0.5742. Right, summary data showing discrimination performance when the switched digit was in the ipsilateral hemisphere, 1st column (motor vs limb), 0.5930 ± 0.0462; one sample t-test vs 0.5, p = 0.0786. 2nd column (limb vs trunk), 0.6600 ± 0.0620; one sample t-test vs 0.5, p = 0.0494. 3rd column (trunk vs visual), 0.6022 ± 0.0196; one sample t-test vs 0.5, p = 0.0008. One-way ANOVA, Sidak's multiple comparisons test, 1st vs 2nd column, p = 0.6523; 1st vs 3rd column, p = 0.9978; 2nd vs 3rd column, p = 0.7640. (**f**) Left, example of a target stimulation for mice to discriminate the target against each individual digit within it. Right, summary data of performance, 1st stim. (target vs 1st digit of the target), 0.6893 ± 0.0196; one sample t-test vs 0.5, $p < 0.0001$. 2nd stim., 0.7911 ± 0.0703; one sample t-test vs 0.5, p = 0.0033. 3rd stim., 0.7600 ± 0.0428; one sample t-test vs 0.5, p = 0.0017. 4th stim., 0.9020 ± 0.0132; one sample t-test vs 0.5, $p < 0.0001$. One-way ANOVA, Sidak's multiple comparisons test, 1st vs 2nd stim., p = 0.3006; 1st vs 3rd stim., p = 0.8439; 1st vs 4th stim., p = 0.0164; 2nd vs 3rd stim., p = 0.9991; 2nd vs 4th stim., p = 0.6932; 3rd vs 4th stim., p = 0.5151. (**g**) Left, example of a target for mice to discriminate the target against its first digit, with the initiation site across all cortical regions. Right, summary data of performance, motor (target initiates from the motor cortex), 0.7000 ± 0.0397; one sample t-test vs 0.5, p = 0.0005. somalimb, 0.6355 ± 0.0539; one sample t-test vs 0.5, p = 0.0031. somatrunk, 0.6625 ± 0.0309; one sample t-test vs 0.5, $p < 0.0001$. visual, 0.7497 ± 0.0339; one sample t-test vs 0.5, $p < 0.0001$. One-way ANOVA, Sidak's multiple comparisons test, motor vs somalimb, p = 0.8672; motor vs somatrunk, p = 0.9840; motor vs visual, p = 0.9414; somalimb vs somatrunk, p = 0.9972; somalimb vs visual, p = 0.2442; somatrunk vs visual, p = 0.4324. (**h**) Left, example showing mice discriminate stimulations on the same site with different durations. Right, summary data of performance. 0.3 s (1.2 s target vs 0.3 s like-target), 0.7256 ± 0.0384; one sample t-test vs 0.5, p = 0.0004. 0.6 s, 0.7088 ± 0.0396; one sample t-test vs 0.5, p = 0.0012. 0.9 s, 0.6087 ± 0.0642; one sample t-test vs 0.5, $p < 0.0001$. One-way ANOVA, Sidak's multiple comparisons test, 0.3 s vs 0.6 s, p = 0.9503; 0.3 s vs 0.9 s, p = 0.0003; 0.6 s vs 0.9 s, p = 0.0031. All data are presented as mean ± s.e.m. Dots represent individual sessions of 100 trials. $^{*}p < 0.05$, $^{**}p < 0.01$, $^{***}p < 0.001$, $^{****}p < 0.0001$ for two-sided t-test and multiple comparisons. $^{\#}p < 0.05$, $^{\#\#}p < 0.01$, $^{\#\#\#}p < 0.001$, $^{\#\#\#\#}p < 0.0001$ for one-sample t-test vs 0.5.

nature portfolio

Corresponding author(s): Yiyuan Yang; Abraham Vázquez-Guardado; Yonggang Huang; Yevgenia Kozorovitskiy; John A Rogers

Last updated by author(s): Oct 1, 2025

Reporting Summary

Nature Portfolio wishes to improve the reproducibility of the work that we publish. This form provides structure for consistency and transparency in reporting. For further information on Nature Portfolio policies, see our Editorial Policies and the Editorial Policy Checklist.

Statistics

For all statistical analyses, confirm that the following items are present in the figure legend, table legend, main text, or Methods section.

n/a	Confirmed	
☐	☒	The exact sample size (*n*) for each experimental group/condition, given as a discrete number and unit of measurement
☐	☒	A statement on whether measurements were taken from distinct samples or whether the same sample was measured repeatedly
☐	☒	The statistical test(s) used AND whether they are one- or two-sided *Only common tests should be described solely by name; describe more complex techniques in the Methods section.*
☐	☒	A description of all covariates tested
☐	☒	A description of any assumptions or corrections, such as tests of normality and adjustment for multiple comparisons
☐	☒	A full description of the statistical parameters including central tendency (e.g. means) or other basic estimates (e.g. regression coefficient) AND variation (e.g. standard deviation) or associated estimates of uncertainty (e.g. confidence intervals)
☐	☒	For null hypothesis testing, the test statistic (e.g. *F*, *t*, *r*) with confidence intervals, effect sizes, degrees of freedom and *P* value noted *Give P values as exact values whenever suitable.*
☒	☐	For Bayesian analysis, information on the choice of priors and Markov chain Monte Carlo settings
☒	☐	For hierarchical and complex designs, identification of the appropriate level for tests and full reporting of outcomes
☐	☒	Estimates of effect sizes (e.g. Cohen's *d*, Pearson's *r*), indicating how they were calculated

Our web collection on statistics for biologists contains articles on many of the points above.

Software and code

Policy information about availability of computer code

Data collection	ABAQUS (ABAQUS Analysis User's Manual, 2020, Dassault Systemes Simulia Corp) was used for mechanical and thermal simulation. COMSOL (COMSOL 6.0, equation Based Modeling User's guide) was used for electromagnetic and optical modeling. Integrating sphere photodiode power meter (S140C, Thorlabs Inc. Newton, NJ) and a calibrated power meter (PM100D, Thorlabs Inc.) were used to collect optical light intensity. Digital multimeter (USB-4065, National Instruments, Austin, TX) was used to collect resistance changes in the thin-film thermistor. An FEI Quanta 650 environmental scanning electron microscope was used to examine the surface morphology of the μ-ILED array and serpentine interconnects. Mediso Nucline v2.01 was used to collect MicroCT imaging data. Olympus VS120 system (Olympus Scientific Solutions Americas) was used to collect histological images. Confocal images were acquired using an Olympus FV3000 confocal microscope or a Leica SP8 confocal microscope with 60x/63x objectives (oil immersion). 30-khz continuous extracellular activity was simultaneously recorded from the multielectrode array and the current source using an OpenEphys data acquisition board with their provided software (OpenEphys, GUI version 0.5.5). The open-source mouse operant chamber (Bpod, Sanworks LLC, NY, developed by Josh Sanders) was used to collect operant learning results. Matlab (R2023a, MathWorks, Natick, MA) was used to control Bpod and the near field communication protocols.
Data analysis	Group statistical analyses were done using GraphPad Prism 7 software (GraphPad, LaJolla, CA). All image data were processed by using FIJI (ImageJ 1.52p) (Schindelin et al., 2012). MicroCT imaging data were processed with Amira v2020.2. Electrophysiology data, operant learning performance, and behavioral analyses were done with Python 3.9 (Python Software Foundation). For spike analysis, stimulation and common-mode artifacts were removed using a version of the ERAASR algorithm (Pachitariu et al., 2024).

The cleaned signal was then acausally filtered with a 300-6,000 Hz bandpass Butterworth filter and sorted using the Kilosort4 Python package (Siegle et al., 2017).
All computer code and customized software generated during and/or used in the current study are available at 10.5281/zenodo.14880024.

For manuscripts utilizing custom algorithms or software that are central to the research but not yet described in published literature, software must be made available to editors and reviewers. We strongly encourage code deposition in a community repository (e.g. GitHub). See the Nature Portfolio guidelines for submitting code & software for further information.

Data

Policy information about availability of data

All manuscripts must include a data availability statement. This statement should provide the following information, where applicable:

- Accession codes, unique identifiers, or web links for publicly available datasets
- A description of any restrictions on data availability
- For clinical datasets or third party data, please ensure that the statement adheres to our policy

Raw data generated during the current study are available from the corresponding author on reasonable request. The analyzed data are available at doi.org/10.5281/zenodo.14880024. Source data that support the findings of this study are included within this paper and its Supplementary Information files.

Research involving human participants, their data, or biological material

Policy information about studies with human participants or human data. See also policy information about sex, gender (identity/presentation), and sexual orientation and race, ethnicity and racism.

Reporting on sex and gender	No human participants are involved in this study.
Reporting on race, ethnicity, or other socially relevant groupings	No human participants are involved in this study.
Population characteristics	No human participants are involved in this study.
Recruitment	No human participants are involved in this study.
Ethics oversight	No human participants are involved in this study.

Note that full information on the approval of the study protocol must also be provided in the manuscript.

Field-specific reporting

Please select the one below that is the best fit for your research. If you are not sure, read the appropriate sections before making your selection.

☒ Life sciences ☐ Behavioural & social sciences ☐ Ecological, evolutionary & environmental sciences

For a reference copy of the document with all sections, see nature.com/documents/nr-reporting-summary-flat.pdf

Life sciences study design

All studies must disclose on these points even when the disclosure is negative.

Sample size	Required sample sizes were estimated based on previous report of published results and our past experience performing similar experiments. No statistical methods were used to pre-determine sample sizes but our sample sizes are similar to those reported in previous publications (Shin et al, 2017; Wu et al, 2021; Yang et al, 2021; Wu et al, 2022).
Data exclusions	No data were excluded from the analysis.
Replication	The number of replicates for each experiment were reported in the paper and the method section. All experiments were repeated at least twice. All attempts at replication were successful.
Randomization	Animals were randomly assigned to treatment groups. All samples were randomly assigned to experimental groups.
Blinding	Blinding was not relevant to the study, as all metrics were quantified and analyzed using automated pipelines applied identically across experimental groups.

Reporting for specific materials, systems and methods

We require information from authors about some types of materials, experimental systems and methods used in many studies. Here, indicate whether each material, system or method listed is relevant to your study. If you are not sure if a list item applies to your research, read the appropriate section before selecting a response.

Materials & experimental systems

n/a	Involved in the study
☒	☐ Antibodies
☒	☐ Eukaryotic cell lines
☒	☐ Palaeontology and archaeology
☐	☒ Animals and other organisms
☒	☐ Clinical data
☒	☐ Dual use research of concern
☒	☐ Plants

Methods

n/a	Involved in the study
☒	☐ ChIP-seq
☒	☐ Flow cytometry
☒	☐ MRI-based neuroimaging

Animals and other research organisms

Policy information about studies involving animals; ARRIVE guidelines recommended for reporting animal research, and Sex and Gender in Research

Laboratory animals	Wild-type C57BL/6 mice were obtained from Charles River (Wilmington, MA) and bred in-house. Adult male and female mice, aged between postnatal days 80 to 120 and weighing 20 to 30 g at the onset of experiments, were used in the study.
Wild animals	No wild animals were used in the study.
Reporting on sex	Sex was not considered in the study design. Male mice were used in the operant learning experiment. Approximately equal numbers of males and females were used in other experiments.
Field-collected samples	No field collected samples were used in the study.
Ethics oversight	Animals were handled according to protocols approved by the Animal Care and Use Committees at Northwestern University.

Note that full information on the approval of the study protocol must also be provided in the manuscript.

Plants

Seed stocks	N/A
Novel plant genotypes	N/A
Authentication	N/A